



# Insight into the design of a Ti<sub>3</sub>C<sub>2</sub> MXene/Ti<sub>4</sub>O<sub>7</sub> composite ceramic membrane boosts the electrocatalytic activity for 1,4-dioxane electro-oxidation

Kuanchang He<sup>a</sup>, Wei Li<sup>a,\*</sup>, Longxiang Tang<sup>a</sup>, Lingyu Chen<sup>a</sup>, Gang Wang<sup>b</sup>, Qian Liu<sup>a</sup>, Xiaodong Xin<sup>a</sup>, Cao Yang<sup>a</sup>, Zhenbei Wang<sup>c</sup>, Sihao Lv<sup>a</sup>, Defeng Xing<sup>d,\*</sup>

<sup>a</sup> Research Center for Eco-environmental Engineering, Dongguan University of Technology, Dongguan 523808, China

<sup>b</sup> School of Environment and Civil Engineering, Dongguan University of Technology, Dongguan 523808, China

<sup>c</sup> Beijing Key Lab for Source Control Technology of Water Pollution, College of Environmental Science and Engineering, Beijing Forestry University, Beijing 100083, China

<sup>d</sup> State Key Laboratory of Urban Water Resource and Environment, School of Environment, Harbin Institute of Technology, Harbin 150090, China

## ARTICLE INFO

### Keywords:

Electrochemical advanced oxidation process  
Ti<sub>3</sub>C<sub>2</sub> MXene  
Ti<sub>4</sub>O<sub>7</sub> ceramic membrane  
Hydroxyl radical  
Refractory organic compounds

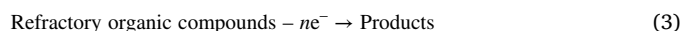
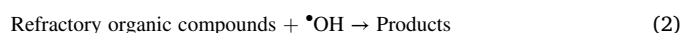
## ABSTRACT

Efficient refractory organic compound (ROC) removal through Ti<sub>4</sub>O<sub>7</sub> ceramic membrane in electrochemical advanced oxidation processes (EAOPs) requires high electrochemical reactivity and stability. Herein, we report on the synthesis and properties of Ti<sub>3</sub>C<sub>2</sub> MXene-doped Ti<sub>4</sub>O<sub>7</sub> ceramic membranes (Ti<sub>3</sub>C<sub>2</sub>@Ti<sub>4</sub>O<sub>7</sub>) using a spark plasma sintering system, after employing density functional theory calculations to design the electrocatalyst. Doping with Ti<sub>3</sub>C<sub>2</sub> MXene resulted in interfacial Ti–O–Ti chemical bond formation, which greatly improved the electronic structure and the generation of hydroxyl radicals (<sup>•</sup>OH). Compared with pristine Ti<sub>4</sub>O<sub>7</sub>, the charge-transfer resistance of Ti<sub>3</sub>C<sub>2</sub>@Ti<sub>4</sub>O<sub>7</sub> decreased from 59.09 to 4.21 Ω, and the <sup>•</sup>OH generation rate enhanced 2.3 – 2.6-fold. Ti<sub>3</sub>C<sub>2</sub>@Ti<sub>4</sub>O<sub>7</sub> could effectively remove 1,4-Dioxane from natural groundwater, and the residual 1,4-Dioxane concentration met the requirements for drinking water. Our study provides a proof-of-concept demonstration using Ti<sub>3</sub>C<sub>2</sub> MXene to manufacture a doped Ti<sub>4</sub>O<sub>7</sub> ceramic membrane for effective ROC removal. The theoretical predictions from this study can inspire novel electrocatalyst designs for EAOPs.

## 1. Introduction

1,4-Dioxane (1,4-D) has been widely utilized as an industrial stabilizer for chlorinated solvents, posing significant environmental pollution risks and possible carcinogenic risks for humans [1,2]. Contamination of groundwater by 1,4-Dioxane necessitates significant attention owing to its notable mobility and high level of toxicity [3]. Chemical oxidation, that is, advanced oxidation processes (AOPs), can effectively decompose 1,4-D through the produced hydroxyl radicals (<sup>•</sup>OH) and has attracted increasing attention. However, the costly and inconvenient operation due to the requirement for constant addition of chemicals for <sup>•</sup>OH generation limits the application of AOPs [4]. Recently, electrochemical advanced oxidation processes (EAOPs) have become popular as promising and efficient techniques to achieve the removal of refractory organic compounds (ROCs); these processes are cost-effective and can be more easily regulated compared with AOPs [5–8]. EAOPs primarily decompose ROCs through two pathways, indirect oxidation via in situ

electrogenerated <sup>•</sup>OH (Eqs. 1 and 2) and direct oxidation of contaminants via direct electron transfer (DET) (Eq. 3) [9,10].



It is worth noting that the anodes play a decisive role in EAOPs, and the ideal anode materials are expected to possess abundant active surface sites for <sup>•</sup>OH generation, excellent interfacial charge-transfer rates, and high stability [11].

Recent studies reported that porous Magnéli phase Ti<sub>4</sub>O<sub>7</sub> ceramic electrodes with adjustable pore sizes, outstanding conductivity comparable to that of metals (~1050 S/cm), excellent corrosion resistance, and high oxygen evolution potential (>2.5 V vs SHE) can be used as promising anodes for the mineralization of organic compounds [12–14]. In

\* Corresponding authors.

E-mail addresses: [liwei@dgut.edu.cn](mailto:liwei@dgut.edu.cn) (W. Li), [dxing@hit.edu.cn](mailto:dxing@hit.edu.cn) (D. Xing).

<https://doi.org/10.1016/j.apcatb.2023.123077>

Received 22 November 2022; Received in revised form 11 June 2023; Accepted 6 July 2023

Available online 7 July 2023

0926-3373/© 2023 Elsevier B.V. All rights reserved.

addition, the affordability, good stability, and nontoxicity of  $\text{Ti}_4\text{O}_7$  electrodes also contribute to their potential to become ideal anode candidate materials compared with other “non-active” materials, including boron-doped diamond (BDD), doped  $\text{SnO}_2$ , and  $\text{PbO}_2$  [15,16]. However, it was found that pure  $\text{Ti}_4\text{O}_7$  exhibits poor electron mobility and  $\cdot\text{OH}$  yield due to high charge-transfer resistance and the lack of reactive sites, which limits its electrochemical reactivity [7]. Thus, to improve the  $\text{Ti}_4\text{O}_7$  electrodes for enhanced contaminant oxidation, two approaches could be used: (i) increasing the effective electroactive surface area and the number of reactive sites [17] and (ii) decreasing the charge-transfer resistance. These approaches are important to improve the  $\cdot\text{OH}$  yield on the surface of  $\text{Ti}_4\text{O}_7$  crystals and the DET process [12]. The doping technology is an effective interface engineering strategy that has been used to achieve these goals. For instance, Xie et al. reported that a significant increase in interfacial electron transfer was achieved by introducing a small amount (0.1 wt%) of carbon materials (carbon black, carbon nanotubes, and graphene) into the  $\text{Ti}_4\text{O}_7$  electrodes, which was attributed to the oxygen-containing functional groups promoting the moderate oxidation of the carbon groups, which increases the electron mobility [13]. Li et al. reported that  $\text{Ti}_4\text{O}_7$  electrodes doped with graphene oxide nanoparticles (GONs) could increase the electroactive surface area and the density of reactive sites at the electrode surface, reaching a kinetic decomposition rate for the 1,4-D electro-oxidation similar to that of BDD ( $1.49$  vs  $1.79 \times 10^{-2} \text{ min}^{-1}$ ) due to the strong chemical interaction of the components via GON–O–Ti bonds [11]. While some studies have addressed the two issues to a certain extent, realizing highly efficient, stable, and large-scale  $\text{Ti}_4\text{O}_7$  electrodes remains challenging due to (i) the lack of selective surface functionalities to establish strong connections for accelerated interfacial charge transfer, (ii) inefficient electron shuttling within the electrocatalysts because of the destruction of  $\pi$ -conjugated systems (e.g., graphene oxide), and (iii) incomplete rational design and regulation of the nanostructures with the reactive sites of the heterogeneous catalysts. Thus, a new type of material has to be developed as the next-generation catalyst for advancing the application of  $\text{Ti}_4\text{O}_7$  electrodes to the wastewater treatment.

MXenes, a class of two-dimensional (2D) inorganic compounds like metal carbides, nitrides, and carbonitrides, exhibit distinguished properties including (i) numerous hydrophilic functionalities, such as  $-\text{O}$  and  $-\text{OH}$  at the surface, which promote strong connections with various electrode substrates [18,19], (ii) outstanding metallic conductivity, which enables super-efficient charge transfer [20], and (iii) exposed terminal metal sites (e.g., Ti), possibly resulting in a much higher electrochemical reactivity than that of carbon materials [21]. These advantageous properties could be harnessed to overcome the above issues. Thus, MXene is a promising material to be employed in EAOPs. Although MXene doping technologies have been reported regarding membrane technologies [22] and photocatalysis [23], to the best of our knowledge, MXene acting as an electrocatalyst doped into  $\text{Ti}_4\text{O}_7$  electrodes for ROC electro-oxidation has not yet been investigated.

Herein, we first utilized density functional theory (DFT) calculations to explore the potential of MXene as an EAOP electrocatalyst. Based on the theoretical studies, we report an interface engineering strategy to fabricate a highly electrocatalytically active and stable MXene ( $\text{Ti}_3\text{C}_2$ )-doped  $\text{Ti}_4\text{O}_7$  electrode ( $\text{Ti}_3\text{C}_2@ \text{Ti}_4\text{O}_7$ ) to promote the electro-oxidation of 1,4-D. The mechanisms behind this high electrocatalytic activity and stability were studied via both theoretical and experimental methods. In addition, the 1,4-D oxidation performance of pristine  $\text{Ti}_4\text{O}_7$  and  $\text{Ti}_3\text{C}_2@ \text{Ti}_4\text{O}_7$  electrodes was evaluated using simulated samples and natural groundwater spiked with 0.1 mM 1,4-D. This work demonstrates how the MXene doping method can improve the electrocatalytic activity toward the development of an improved  $\text{Ti}_4\text{O}_7$  electrode.

## 2. Materials and methods

### 2.1. Chemicals, materials, and natural groundwater sample

Detailed information is provided in Text S1.

### 2.2. Density functional theory calculations

All DFT calculations were conducted based on the Cambridge Serial Total Energy Package (CASTEP) code [24]. The electron exchange-correlation interactions were described using the generalized gradient approximation (GGA) with the Perdew–Burke–Ernzerhof (PBE) functional [25]. Considering the long-range interaction at the interface, the Tkatchenko–Scheffler method was used to correct the van der Waals interactions. The (0 0 1) plane of  $\text{Ti}_3\text{C}_2$  MXene and the (1  $\bar{2}$  0) plane of  $\text{Ti}_4\text{O}_7$  were adopted as the active facets in this study to build the heterostructures and the slab model [26,27]. The Brillouin zone integration was sampled with the Gamma point-centered mesh due to the large cell ( $a = b = 12.07 \text{ \AA}$ ,  $c = 15.76 \text{ \AA}$ ), and the energy cutoff was set to 550 eV for geometry optimization and calculations through a series of tests (Fig. S1a); the energy cutoff for the pristine  $\text{Ti}_4\text{O}_7$  slab model was also set to 550 eV after the tests (Fig. S1b). The vacuum spacing in the direction perpendicular to the plane of the catalyst was at least  $10 \text{ \AA}$ . During the geometry optimization process, the energy convergence tolerance, maximum force, and maximum displacement were set to  $1 \times 10^{-5} \text{ eV/atom}$ ,  $0.05 \text{ eV/atom}$ , and  $2 \times 10^{-3} \text{ \AA}$ , respectively. For the electronic properties, a Monkhorst–Pack k-point grid ( $2 \times 2 \times 1$ ), which is denser compared with that used for the geometry optimization, was used to calculate the density of states (DOS).

An assessment of the interfacial formation energy ( $E_F$ ) calculated according to Eq. 4 was conducted to verify the thermodynamic stability of the heterostructures [28].

$$E_F = \frac{1}{N_M} (E_{\text{Ti}_3\text{C}_2@ \text{Ti}_4\text{O}_7} - E_{\text{Ti}_3\text{C}_2} - E_{\text{Ti}_4\text{O}_7}) \quad (4)$$

where  $E_{\text{Ti}_3\text{C}_2@ \text{Ti}_4\text{O}_7}$ ,  $E_{\text{Ti}_3\text{C}_2}$ , and  $E_{\text{Ti}_4\text{O}_7}$  represent the total energy of the  $\text{Ti}_3\text{C}_2@ \text{Ti}_4\text{O}_7$  interlayer,  $\text{Ti}_3\text{C}_2$  MXene monolayer, and  $\text{Ti}_4\text{O}_7$  substrate, respectively;  $N_M$  is the total number of the transition metal atoms in each supercell.

The  $\text{H}_2\text{O}$  adsorption energy ( $E_{\text{ads}}$ ) and the  $\cdot\text{OH}$  desorption energy ( $E_{\text{des}}$ ) on the surface of pristine  $\text{Ti}_4\text{O}_7$  and  $\text{Ti}_3\text{C}_2@ \text{Ti}_4\text{O}_7$  were calculated using Eqs. 5 and 6, respectively.

$$E_{\text{ads}} = E_{\text{adsorbate+substrate}} - E_{\text{adsorbate}} - E_{\text{substrate}} \quad (5)$$

$$E_{\text{des}} = E_{\text{adsorbate}} + E_{\text{substrate}} - E_{\text{adsorbate+substrate}} \quad (6)$$

where  $E_{\text{adsorbate+substrate}}$ ,  $E_{\text{adsorbate}}$ , and  $E_{\text{substrate}}$  represent the total energy of the adsorbate–substrate material, adsorbate ( $\text{H}_2\text{O}$  or  $\cdot\text{OH}$ ), and substrate (pristine  $\text{Ti}_4\text{O}_7$  or  $\text{Ti}_3\text{C}_2@ \text{Ti}_4\text{O}_7$ ), respectively.

The reaction energy ( $E_r$ ) for the transformation of the adsorbed OH group on the surface ( $\cdot\text{OH}$ ) into the adsorbed  $\cdot\text{OH}$  ( $\cdot\text{OH}$ ) was defined according to Eq. 7.

$$E_r = E_{\cdot\text{OH}} - E_{\cdot\text{OH}} \quad (7)$$

where  $E_{\cdot\text{OH}}$  and  $E_{\cdot\text{OH}}$  represent the total energy of  $\cdot\text{OH}$  including the substrate and  $\cdot\text{OH}$  including the substrate, respectively. The initial spin of the radical system was set to 1 [29].

The Gibbs free energy ( $\Delta G$ ) calculations were conducted with cutoff kinetic energy of 400 eV, and the *vander Waals* interaction was described using the DFT-D2 method which was proposed by Grimme. The calculations were carried out based on Eq. 8.

$$\Delta G = \Delta E + \Delta E_{\text{ZPE}} - T\Delta S \quad (8)$$

where  $\Delta E$ ,  $\Delta E_{\text{ZPE}}$ , and  $\Delta S$  represent the total energy difference, the

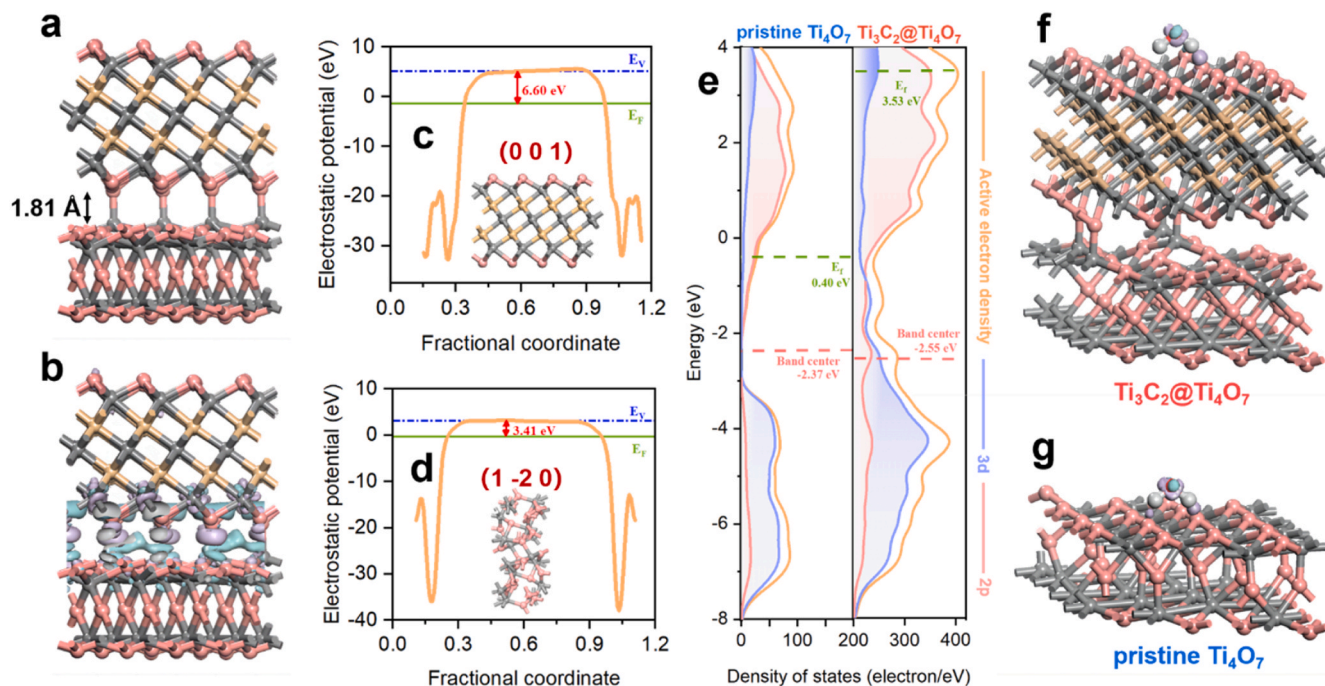
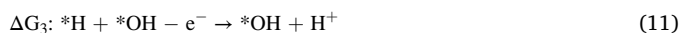


**Fig. 1.** DFT calculations of the  $\text{Ti}_3\text{C}_2@\text{Ti}_4\text{O}_7$  and pristine  $\text{Ti}_4\text{O}_7$  structures. (a) Geometry configuration of O-terminated  $\text{Ti}_3\text{C}_2@\text{Ti}_4\text{O}_7$  with an interfacial spacing of 1.81 Å. The pink, gray, and yellow balls represent the O, Ti, and C atoms, respectively. (b) Electron density isosurface of the  $\text{Ti}_3\text{C}_2@\text{Ti}_4\text{O}_7$  interface; light purple and light blue represent electron accumulation and depletion, respectively. (c, d) Work functions of  $\text{Ti}_3\text{C}_2$  MXene and  $\text{Ti}_4\text{O}_7$ ; the blue dashed line and the light green line represent the vacuum energy level and the Fermi level, respectively. (e) DOS and PDOS calculated for  $\text{Ti}_3\text{C}_2@\text{Ti}_4\text{O}_7$  and pristine  $\text{Ti}_4\text{O}_7$ ; the pink and light green lines represent the band center (p band + d band) and the Fermi level, respectively. (f, g) Electron density distribution of  $\text{H}_2\text{O}$  adsorbed on the  $\text{Ti}_3\text{C}_2@\text{Ti}_4\text{O}_7$  and pristine  $\text{Ti}_4\text{O}_7$  structures; light purple and light blue represent electron accumulation and depletion, respectively.

changes of zero-point vibration energy, and entropy energy between reactants and products. The equations displayed below are the calculation steps of  $\text{H}_2\text{O}$  activation on the surfaces of  $\text{Ti}_3\text{C}_2@\text{Ti}_4\text{O}_7$  and pristine  $\text{Ti}_4\text{O}_7$  (Eq. 9–12) [30].



### 2.3. Electrode synthesis

The synthesis method of oxygen-rich terminal  $\text{Ti}_3\text{C}_2$  MXene was proposed by Sun et al. [31] and Ran et al. [32].  $\text{Ti}_3\text{AlC}_2$  powder (1 g) was immersed in 49% HF (10 mL) for 36 h at 35 °C under constant stirring to selectively remove all the Al species in  $\text{Ti}_3\text{AlC}_2$ . The mixture was washed using deionized (DI) water until a transparent supernatant was obtained. Subsequently, the as-synthesized sediment was centrifuged and dried in vacuum at 80 °C overnight. To maximize the number of oxygen terminals of  $\text{Ti}_3\text{C}_2$  MXene, the dried sediment was annealed in air for 2 h at 200 °C in a muffle furnace to transform the  $-\text{OH}$  and  $-\text{F}$  terminations into  $-\text{O}$  terminations. 100 mg of the O-terminated  $\text{Ti}_3\text{C}_2$  MXene was taken out of the furnace and mixed with 100 mL of DI water. The mixture was ultrasonicated for 8 h and centrifuged at 13000 rpm to obtain the O-terminated  $\text{Ti}_3\text{C}_2$  MXene nanosheets in the supernatant, and its concentration was determined to be 0.11 mg/mL.

Then, 1.5 g of the  $\text{Ti}_4\text{O}_7$  powder with or without 1–5 wt%  $\text{Ti}_3\text{C}_2$  MXene was added to 100 mL of ethanol, dispersed in an ultrasonic bath for 40 min to obtain a fine powder mixture, and magnetically stirred (IKA RCT basic, Germany) at 800 rpm for 30 min to obtain a suspension. The solvent was removed in vacuum (LabServ™ 20, Thermo Fisher

Scientific, USA) at 80 °C for 24 h. Subsequently, the dried materials were transferred to the cylindrical mold (area: 3.14 cm<sup>2</sup>; thickness: 1.5 mm) of a spark plasma sintering (SPS) system (SPS-212HF, Fuji Electronic Industrial Co., Ltd., Japan) to synthesize ceramic membranes consisting of X%  $\text{Ti}_3\text{C}_2@\text{Ti}_4\text{O}_7$  (X% = 1–5 wt%) and pristine  $\text{Ti}_4\text{O}_7$ . The details of the sintering process are provided in Text S2. The images of the as-synthesized 2%  $\text{Ti}_3\text{C}_2@\text{Ti}_4\text{O}_7$  are shown in Fig. S2, and the X%  $\text{Ti}_3\text{C}_2@\text{Ti}_4\text{O}_7$  and pristine  $\text{Ti}_4\text{O}_7$  ceramics were polarized at  $-2.0$  V vs SCE for 2 h.

### 2.4. Physicochemical characterization

X-ray diffraction (XRD) patterns were obtained using a D8-Advance diffractometer (Bruker, Germany) with Cu K $\alpha$  radiation. Scanning electron microscopy (SEM) and energy-dispersive X-ray spectroscopy (EDS) were performed using an FEI Quanta 450 instrument (Thermo Fisher Scientific, USA). A JEM-2100 microscope (JEOL, Japan) was used to conduct transmission electron microscopy (TEM), and high-resolution transmission electron microscopy (HRTEM, FEI Tecnai G2 F30, Thermo Fisher Sci., USA). The surface chemical compositions were analyzed via X-ray photoelectron spectroscopy (XPS) using an ESCA Lab 250Xi instrument (Thermo Fisher Scientific, USA). Raman spectra were acquired using an inVia spectrophotometer (Renishaw, UK). Atomic force microscopy (AFM) was conducted using a Multimode 8 system (Bruker, Germany). The porosimetry distribution of the electrodes was investigated using an Autopore IV mercury porosimeter (Micromeritics, USA). The experimental work function (WF) was measured via ultraviolet photoelectron spectroscopy (UPS) using an X-ray photoelectron spectrometer (Thermo ESCALAB 250XI, USA).

### 2.5. Electrochemical measurements

Electrochemical characterizations, such as electrochemical impedance spectroscopy (EIS) and cyclic voltammetry (CV), were conducted



using an AutoLab M204 electrochemical workstation (Metrohm, Switzerland). A platinum foil and a saturated calomel electrode (SCE) were employed as the counter electrode and the reference electrode, respectively. EIS was performed in the frequency range between 10 kHz and 0.01 Hz, and the NOVA software was used for data acquisition. The Nyquist curves were fitted using the Zview software. The CV plots were recorded at scan rates varying between 5 and 100 mV/s.

## 2.6. Experimental procedures

Unless otherwise stated, all electrochemical experiments were conducted in batch mode using a cylindrical reactor with 60 mL of an aqueous 0.1 mM 1,4-D solution containing 100 mM  $\text{Na}_2\text{SO}_4$  as the electrolyte at an applied current ( $j$ ) of 20  $\text{mA}/\text{cm}^2$  (Fig. S3).  $\text{Ti}_3\text{C}_2@/\text{Ti}_4\text{O}_7$  or pristine  $\text{Ti}_4\text{O}_7$  served as the anode, while a cylindrical  $\text{RuO}_2/\text{IrO}_2$  electrode (area: 3.14  $\text{cm}^2$ ; thickness: 1.3 mm) was used as the cathode, and the anode–cathode spacing was 1.2 cm. Probe tests were conducted to assess the DET process and  $\cdot\text{OH}$  generation. Oxalic acid (OA, 1 mM) was employed to estimate the DET process contribution to contaminant oxidation. Coumarin (COU, 1 mM), *p*-benzoquinone (*p*-BQ, 3 mM), and terephthalic acid (TA, 1 mM) were selected to evaluate the  $\cdot\text{OH}$  production rates. 1,4-D oxidations were conducted under constant stirring at 800 rpm. Quenching experiments were carried out to scavenge  $\cdot\text{OH}$  using methyl alcohol (MeOH, 10–100 mM) to investigate the contribution of radicals to ROC removal. The effect of the doping amount of  $\text{Ti}_3\text{C}_2$  MXene on the 1,4-D degradation rate constants was evaluated. The influence of different water matrices on 1,4-D decomposition in the presence of  $\text{Cl}^-$ ,  $\text{HCO}_3^-$ ,  $\text{H}_2\text{PO}_4^-$ , and  $\text{NO}_3^-$  anions in the concentration range of 0.5–10 mM was studied. 1,4-D removal from natural groundwater was conducted to explore the application feasibility of the proposed electrode, and the characteristics of this water source are presented in Table S1. All instrumental analyses are described in Text S3.

## 3. Results and discussion

### 3.1. Mechanistic investigation of $\text{Ti}_3\text{C}_2$ MXene as an electrocatalyst doped into a $\text{Ti}_4\text{O}_7$ electrode

An excellent electrocatalyst should possess a high stability, fast electron transfer, and a strong ability to produce  $\cdot\text{OH}$ . To investigate the feasibility of employing  $\text{Ti}_3\text{C}_2$  MXene as a highly efficient electrocatalyst doped into a  $\text{Ti}_4\text{O}_7$  electrode to improve the electrocatalytic activity, mechanistic investigations using DFT calculations have been conducted [33]. In  $\text{Ti}_3\text{C}_2$  MXene, both O- and OH-terminated configurations endow the material with a strong adsorption ability and an efficient activation of  $\text{H}_2\text{O}$  [34], which may greatly improve the production of  $\cdot\text{OH}$  for ROC removal. Therefore, DFT calculations of  $\text{Ti}_3\text{C}_2@/\text{Ti}_4\text{O}_7$  were conducted based on the models exhibiting hydrophilic functionalities.

#### 3.1.1. Geometry optimization of the $\text{Ti}_3\text{C}_2@/\text{Ti}_4\text{O}_7$ heterostructures

Firstly, we evaluated the feasibility and stability of O- and OH-terminated  $\text{Ti}_3\text{C}_2@/\text{Ti}_4\text{O}_7$ . Interestingly, as shown in Fig. 1a, a new chemical Ti–O–Ti bond between the Ti and O atoms of  $\text{Ti}_3\text{C}_2$  MXene and the Ti atoms of  $\text{Ti}_4\text{O}_7$  was found in the optimized O-terminated  $\text{Ti}_3\text{C}_2@/\text{Ti}_4\text{O}_7$ , implying the possible chemical interaction between  $\text{Ti}_3\text{C}_2$  MXene and  $\text{Ti}_4\text{O}_7$ . Furthermore, the energy of both structures converged, and the two structures did not show any obvious deformation; the interlayer distances were 1.81 and 1.76 Å (Fig. 1a and Fig. S4a). The  $E_F$  of O-terminated  $\text{Ti}_3\text{C}_2@/\text{Ti}_4\text{O}_7$  was  $-0.60$  eV, which was much lower than that of OH-terminated  $\text{Ti}_3\text{C}_2@/\text{Ti}_4\text{O}_7$  ( $-0.15$  eV) (Table S2). The negative  $E_F$  proved that the two configurations were energetically stable and the fabrication of  $\text{Ti}_3\text{C}_2@/\text{Ti}_4\text{O}_7$  was feasible. However,  $\text{Ti}_3\text{C}_2@/\text{Ti}_4\text{O}_7$  was more likely to exist in the form of the O-terminated configuration due to its lower  $E_F$ , which was also consistent with a previous study [35]. Thus, the subsequent property calculations were

conducted on O-terminated  $\text{Ti}_3\text{C}_2@/\text{Ti}_4\text{O}_7$ . In addition, the slab model of pristine  $\text{Ti}_4\text{O}_7$  was established and optimized (Fig. S4b).

#### 3.1.2. Electronic properties of the $\text{Ti}_3\text{C}_2@/\text{Ti}_4\text{O}_7$ heterostructure

The electron density isosurface of the  $\text{Ti}_3\text{C}_2@/\text{Ti}_4\text{O}_7$  heterostructure exhibited a distinct electron redistribution surrounding the Ti–O–Ti bonds in the interfacial region (Fig. 1b). Numerous electrons gathered at the bottom of  $\text{Ti}_3\text{C}_2$  MXene (light purple region), and substantial electron depletion occurred above  $\text{Ti}_4\text{O}_7$  (light blue region). This revealed that the  $\text{Ti}_3\text{C}_2@/\text{Ti}_4\text{O}_7$  heterostructure could significantly tune the interfacial charge transfer behaviors, resulting in an enhanced electronic transmission from  $\text{Ti}_4\text{O}_7$  to  $\text{Ti}_3\text{C}_2$  MXene [36]. The WF of the two constituents in the heterostructure was also consistent with this finding because electrons move spontaneously from a material with a lower WF value ( $WF_{\text{Ti}_4\text{O}_7} = 3.41$  eV) to another material with a higher WF value ( $WF_{\text{Ti}_3\text{C}_2 \text{ MXene}} = 6.60$  eV) (Fig. 1c and d). A Schottky junction would be formed when the two layers are in close contact with each other to accelerate charge transport and reach electronic equilibrium at the Fermi energy level ( $E_F$ ) [23]. The WF of  $\text{Ti}_3\text{C}_2@/\text{Ti}_4\text{O}_7$  was 4.77 eV, while the WF of slab model of pristine  $\text{Ti}_4\text{O}_7$  was 4.67 eV (Fig. S5a and b). Furthermore, the spectra of the total density of states (TDOS) and projected density of states (PDOS) were explored to gain an in-depth understanding of the electronic structure of  $\text{Ti}_3\text{C}_2@/\text{Ti}_4\text{O}_7$  and pristine  $\text{Ti}_4\text{O}_7$ . It could be seen that the DOS curves resided across the  $E_F$ , indicating that the modeled heterojunction exhibited the metallic nature (Fig. 1e) [37]. In addition, the  $\text{Ti}_3\text{C}_2@/\text{Ti}_4\text{O}_7$  heterostructure possessed a larger  $E_f$  (3.53 eV vs 0.40 eV) and higher DOS values at  $E_f$  relative to those of pristine  $\text{Ti}_4\text{O}_7$ . The above results suggested again that  $\text{Ti}_3\text{C}_2@/\text{Ti}_4\text{O}_7$  exhibited fast electron transport and an excellent electrical conductivity [38–40]. The PDOS curves revealed that the Ti 3d and O 2p orbitals mainly contributed to the active electron density of both  $\text{Ti}_3\text{C}_2@/\text{Ti}_4\text{O}_7$  and pristine  $\text{Ti}_4\text{O}_7$  (Fig. S4c). It was found that the band center of the active electron density (p band and d band) of  $\text{Ti}_3\text{C}_2@/\text{Ti}_4\text{O}_7$  decreased by 0.18 eV compared with that of pristine  $\text{Ti}_4\text{O}_7$  (Fig. 1e), demonstrating the effective regulation of the active electron density and the weakened interactions between the adsorbate and the surface, which was beneficial for  $\cdot\text{OH}$  desorption [41].

#### 3.1.3. Mechanism of $\cdot\text{OH}$ generation via the $\text{Ti}_3\text{C}_2@/\text{Ti}_4\text{O}_7$ heterostructure

To investigate the  $\cdot\text{OH}$  generation ability of  $\text{Ti}_3\text{C}_2@/\text{Ti}_4\text{O}_7$ , the adsorption behaviors of  $\text{H}_2\text{O}$  on  $\text{Ti}_3\text{C}_2@/\text{Ti}_4\text{O}_7$  and pristine  $\text{Ti}_4\text{O}_7$  were studied. As shown in Fig. 1f and g, the significant electron accumulation above the O atoms of  $\text{Ti}_3\text{C}_2$  MXene and pristine  $\text{Ti}_4\text{O}_7$  showed that the electrons were transferred from  $\text{H}_2\text{O}$  to the models. As listed in Table S3,  $E_{\text{ads}}$  of  $\text{H}_2\text{O}$  on the surface of  $\text{Ti}_3\text{C}_2@/\text{Ti}_4\text{O}_7$  was  $-0.44$  eV, while that of pristine  $\text{Ti}_4\text{O}_7$  was 0.26 eV, which was close to the value reported previously [42]. This indicated that  $\text{H}_2\text{O}$  adsorption on  $\text{Ti}_3\text{C}_2@/\text{Ti}_4\text{O}_7$  was energetically more favorable. To form  $\cdot\text{OH}$ , adsorbed  $\text{H}_2\text{O}$  dissociates into OH and H, and then the OH group connected to the electrode surface ( $\cdot\text{OH}$ ) via a physical, weak interaction transforms into  $\cdot\text{OH}$ . Thus, to elucidate the conversion process of  $\cdot\text{OH}$  into  $\cdot\text{OH}$  from a thermodynamics perspective,  $E_r$  was calculated. It was established that the in situ conversion of  $\cdot\text{OH}$  into  $\cdot\text{OH}$  was an exothermic reaction on the surfaces of both  $\text{Ti}_3\text{C}_2@/\text{Ti}_4\text{O}_7$  and pristine  $\text{Ti}_4\text{O}_7$ , as demonstrated by the corresponding  $E_r$  values of  $-0.87$  and  $-0.52$  eV, respectively (Table S3). This further indicated that the  $\cdot\text{OH}$  generation of  $\text{Ti}_3\text{C}_2@/\text{Ti}_4\text{O}_7$  was more viable. The spin density also demonstrated the presence of lone-pair electrons in  $\cdot\text{OH}$  (Fig. S4d and e) [29]. The Gibbs free energies of  $\text{H}_2\text{O}$  activation on the surfaces of  $\text{Ti}_3\text{C}_2@/\text{Ti}_4\text{O}_7$  and pristine  $\text{Ti}_4\text{O}_7$  were obtained (Fig. S6). It could be observed that  $\Delta G_2$  (1.84 eV) and  $\Delta G_4$  (2.57 eV) were much larger than  $\Delta G_1$  ( $-0.11$  eV) and  $\Delta G_3$  ( $-1.47$  eV) during  $\text{H}_2\text{O}$  activation in pristine  $\text{Ti}_4\text{O}_7$ , indicating that the rate-determining steps for  $\cdot\text{OH}$  production on pristine  $\text{Ti}_4\text{O}_7$  surface were the formations of  $\cdot\text{H} + \cdot\text{OH}$  from  $\cdot\text{H}_2\text{O}$  and  $\cdot\text{OH}$  from  $\cdot\text{OH}$ . Meanwhile, the  $\Delta G_4$  for  $\text{Ti}_3\text{C}_2@/\text{Ti}_4\text{O}_7$  was only 0.47 eV although its  $\Delta G_2$  at 1.85 eV was almost identical to  $\Delta G_2$  (1.84 eV) in pristine  $\text{Ti}_4\text{O}_7$ . These



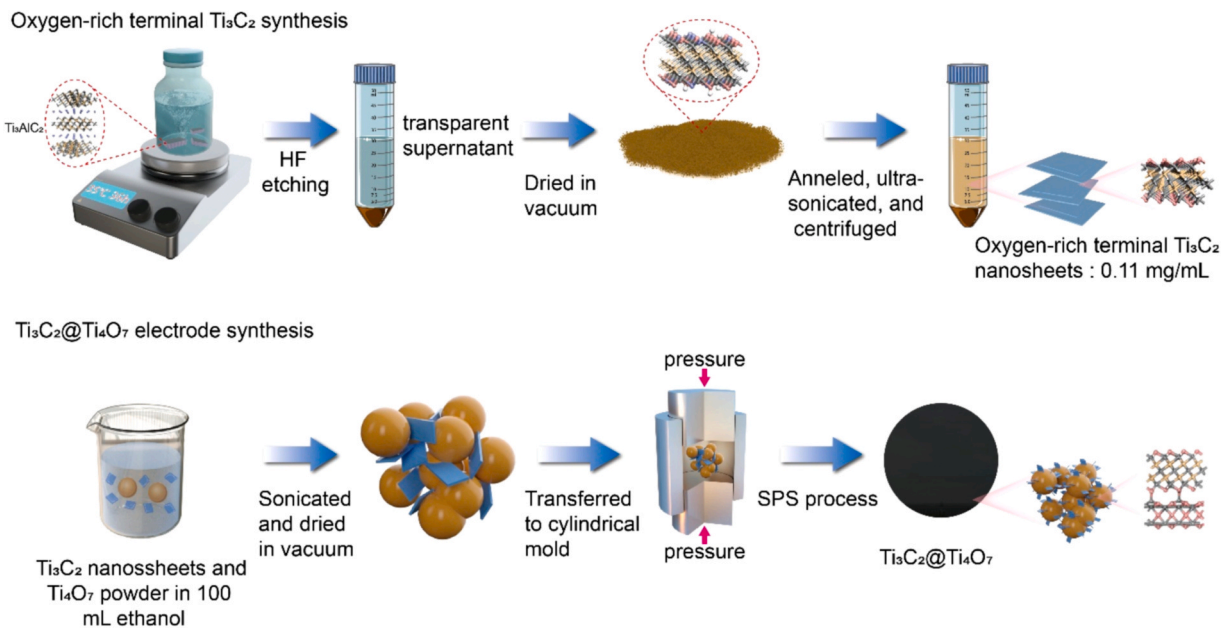


Fig. 2. Schematic of the fabrication of oxygen-rich terminal  $\text{Ti}_3\text{C}_2$  MXene and  $\text{Ti}_3\text{C}_2@ \text{Ti}_4\text{O}_7$ .

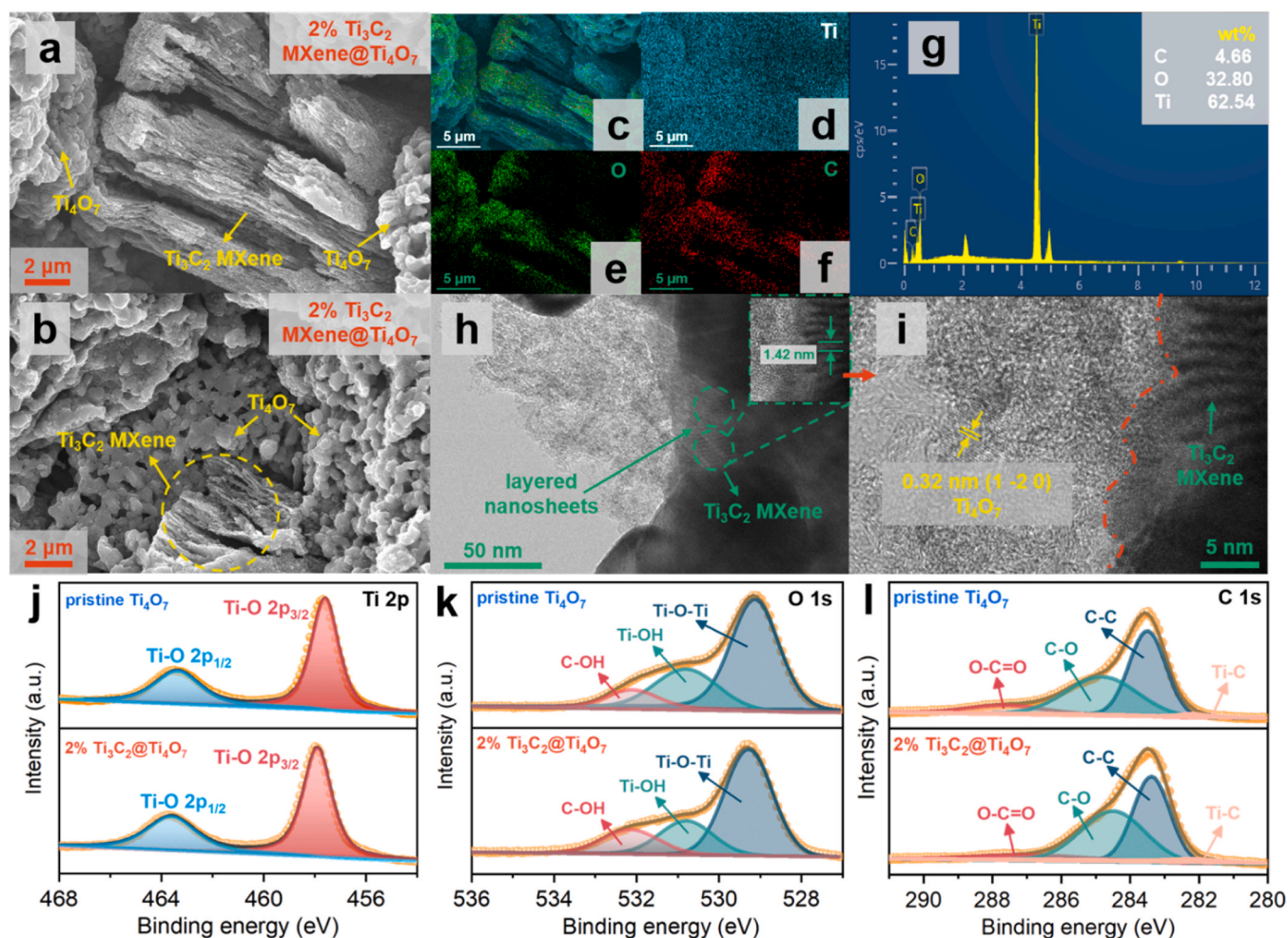
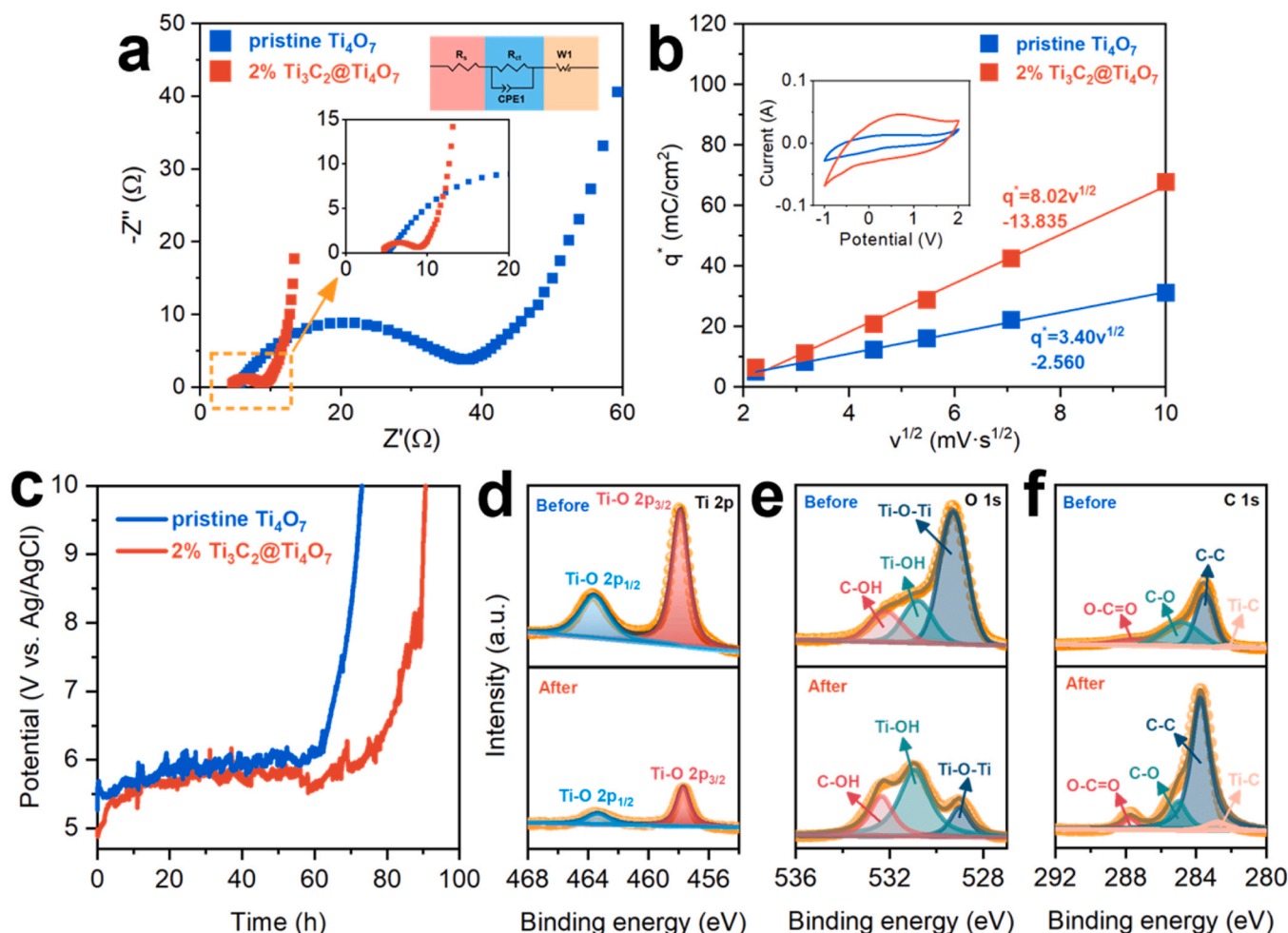


Fig. 3. (a, b) SEM images of 2%  $\text{Ti}_3\text{C}_2@ \text{Ti}_4\text{O}_7$ . (c) EDS elemental distribution of a). (d-f) Corresponding elemental distributions in c) of Ti, O, and C, respectively. (g) EDS surface scan results. (h) TEM image of 2%  $\text{Ti}_3\text{C}_2@ \text{Ti}_4\text{O}_7$ . (i) HRTEM image of 2%  $\text{Ti}_3\text{C}_2@ \text{Ti}_4\text{O}_7$ . (j-l) Ti 2p, O 1s, and C 1s XPS spectra of 2%  $\text{Ti}_3\text{C}_2@ \text{Ti}_4\text{O}_7$ ; the raw XPS data were indicated by the orange dots, and the spectra are calibrated to the C 1s peak at 284.6 eV.



**Fig. 4.** (a) Nyquist curves of 2%  $\text{Ti}_3\text{C}_2/\text{Ti}_4\text{O}_7$  and pristine  $\text{Ti}_4\text{O}_7$ ; the magnified view of the high-frequency region displays the details of the curves, and the inset in the top-right corner shows the equivalent circuit. (b) Linear relationship of the voltammetric charge and the square root of the scan rate (5–100 mV/s); the inset shows the CV plots of 2%  $\text{Ti}_3\text{C}_2/\text{Ti}_4\text{O}_7$  and pristine  $\text{Ti}_4\text{O}_7$  at a scan rate of 30 mV/s. (c) Accelerated service life testing of 2%  $\text{Ti}_3\text{C}_2/\text{Ti}_4\text{O}_7$  and pristine  $\text{Ti}_4\text{O}_7$  in 1 M  $\text{H}_2\text{SO}_4$  at 1 A/cm<sup>2</sup>. (d–f) Ti 2p, O 1s, and C 1s XPS spectra of 2%  $\text{Ti}_3\text{C}_2/\text{Ti}_4\text{O}_7$  before and after the accelerated service life test; the spectra are calibrated to the C 1s peak at 284.6 eV.

results revealed that the introduction of  $\text{Ti}_3\text{C}_2$  MXene could reduce the  $\Delta G_4$  and thus increase the  $\cdot\text{OH}$  production from  $\text{H}_2\text{O}$ . In addition, the decrease of the band center of active electron density of  $\text{Ti}_3\text{C}_2/\text{Ti}_4\text{O}_7$  may prompt the release of  $\cdot\text{OH}$  into solution because more electrons would be drawn from the O 2p orbital compared with the case of pristine  $\text{Ti}_4\text{O}_7$ . The deficient electrons in the O 2p orbital implied a weakened adsorption of  $\cdot\text{OH}$  and were therefore beneficial to  $\cdot\text{OH}$  desorption [43]; this was also demonstrated by the  $E_{\text{des}}$  values of  $\cdot\text{OH}$  in  $\text{Ti}_3\text{C}_2/\text{Ti}_4\text{O}_7$  (−1.46 eV) and pristine  $\text{Ti}_4\text{O}_7$  (−0.03 eV). Based on these theoretical predictions, the advantages of the employment of  $\text{Ti}_3\text{C}_2$  MXene in  $\text{Ti}_4\text{O}_7$  electrode are demonstrated. It can be expected that O-terminated  $\text{Ti}_3\text{C}_2/\text{Ti}_4\text{O}_7$  is capable of producing abundant  $\cdot\text{OH}$  and achieving satisfactory ROC removal. Thus, we should adopt a suitable  $\text{Ti}_3\text{C}_2/\text{Ti}_4\text{O}_7$  electrode synthesis method to maximize the number of −O terminations.

### 3.2. Physical characterization of $\text{Ti}_3\text{C}_2/\text{Ti}_4\text{O}_7$

Guided by the above theoretical calculations,  $\text{Ti}_3\text{C}_2$  MXene nanosheets rich in oxygen terminations were obtained via annealing and strong ultrasonication (Fig. 2a), and X wt%  $\text{Ti}_3\text{C}_2/\text{Ti}_4\text{O}_7$  was fabricated through the SPS process (Fig. 2b). The high-temperature synthesis process was demonstrated to form various interfacial bonds, which enabled the formation of Ti–O–Ti chemical bonds between  $\text{Ti}_3\text{C}_2$  MXene and

$\text{Ti}_4\text{O}_7$  in our work [11,44]. After doping  $\text{Ti}_4\text{O}_7$  with 2% O-terminated  $\text{Ti}_3\text{C}_2$  MXene, it was observed that the multilayered  $\text{Ti}_3\text{C}_2$  MXene nanosheets with uniformly dispersed nanoparticles on their surfaces were surrounded by  $\text{Ti}_4\text{O}_7$ , which retained its original morphology of pristine  $\text{Ti}_4\text{O}_7$  (Fig. 3a and b, Fig. S7). This structural feature is beneficial for increasing the number of edges and defects and improving the electrocatalytic reactions [40]. Furthermore, the introduction of multilayered  $\text{Ti}_3\text{C}_2$  MXene was conducive to modifying the electron delocalization structure, enabling electron transfer at the heterostructure interface [27,45]. EDS mapping demonstrated the successful doping with  $\text{Ti}_3\text{C}_2$  MXene (Fig. 3c–g). The XRD patterns of 2%  $\text{Ti}_3\text{C}_2/\text{Ti}_4\text{O}_7$  and pristine  $\text{Ti}_4\text{O}_7$  were in good agreement with the  $\text{Ti}_4\text{O}_7$  standard characteristic peaks (JCPDS Card No. 50–0787), indicating that the original  $\text{Ti}_4\text{O}_7$  crystal structure was retained in 2%  $\text{Ti}_3\text{C}_2/\text{Ti}_4\text{O}_7$  (Fig. S8) [46], which was consistent with the SEM analyses. However, the characteristic (0 0 2) peak of  $\text{Ti}_3\text{C}_2$  MXene ( $2\theta = 8.9^\circ$ ) was not observed in the XRD pattern of 2%  $\text{Ti}_3\text{C}_2/\text{Ti}_4\text{O}_7$  (Fig. S8) [47]. This might be attributed to the chemical reaction between  $\text{Ti}_3\text{C}_2$  MXene and  $\text{Ti}_4\text{O}_7$  during the synthetic process, implying the possible interface effect in 2%  $\text{Ti}_3\text{C}_2/\text{Ti}_4\text{O}_7$  heterostructure [46]. Confirming the SEM and EDS observations, the coexistence of  $\text{Ti}_3\text{C}_2$  MXene and  $\text{Ti}_4\text{O}_7$  was visible in the TEM image (Fig. 3h), which also clearly displayed the layered nanosheets of  $\text{Ti}_3\text{C}_2$  MXene with an interlayer spacing of  $\sim 1.42$  nm (inset of Fig. 3h). Furthermore, according to the HRTEM image (Fig. 3i),  $\text{Ti}_3\text{C}_2$  MXene was

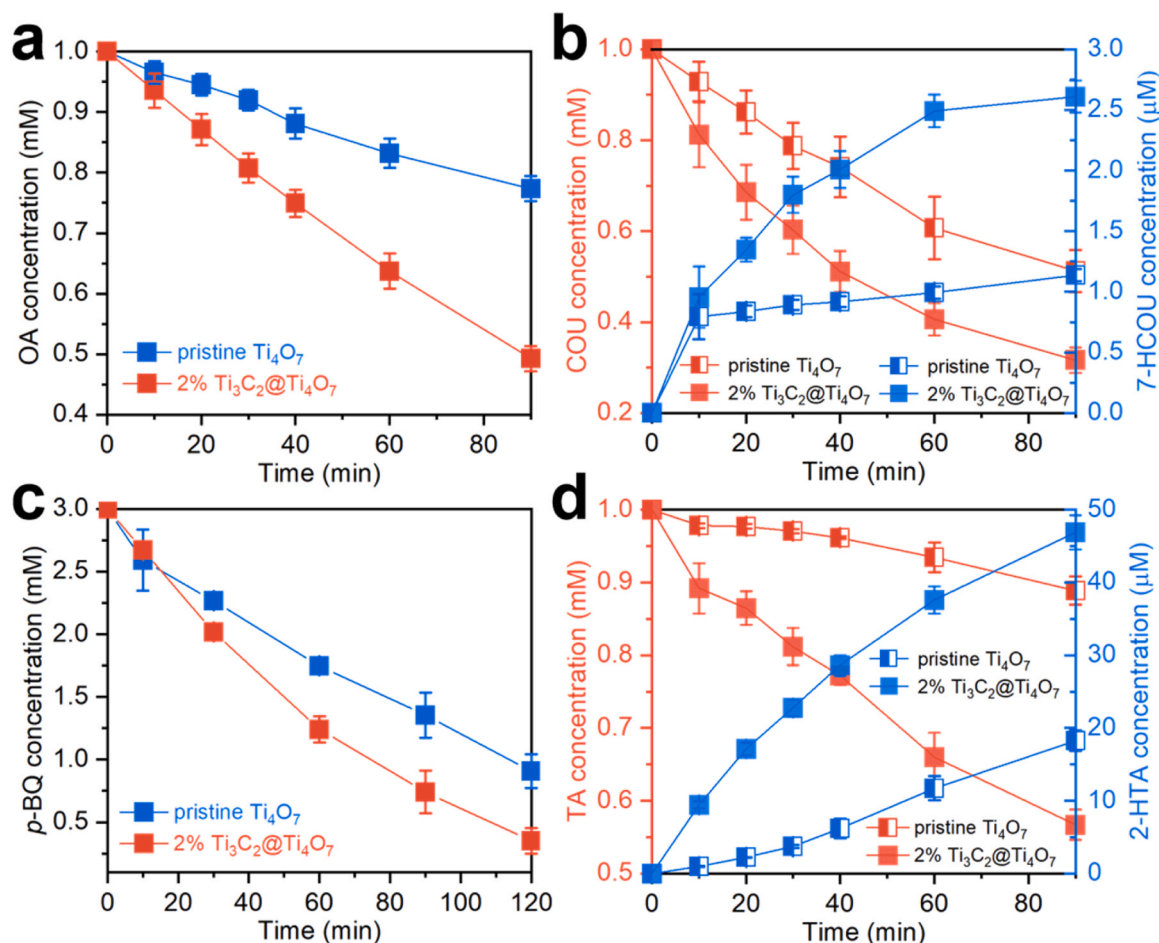


**Fig. 5.** (a, c) Degradation of OA and p-BQ for 2%  $\text{Ti}_3\text{C}_2@\text{Ti}_4\text{O}_7$  and pristine  $\text{Ti}_4\text{O}_7$  ( $[\text{OA}]_0 = 1 \text{ mM}$ ,  $[\text{p-BQ}]_0 = 3 \text{ mM}$ ). (b, d) Degradation of COU and TA for 2%  $\text{Ti}_3\text{C}_2@\text{Ti}_4\text{O}_7$  and pristine  $\text{Ti}_4\text{O}_7$  ( $[\text{COU}]_0 = 1 \text{ mM}$ ,  $[\text{TA}]_0 = 1 \text{ mM}$ ) and formation of their corresponding products, namely 7-HCOU and 2-HTA, respectively. Reaction conditions of (a–d):  $j = 20 \text{ mA/cm}^2$ ,  $[\text{Na}_2\text{SO}_4] = 100 \text{ mM}$ .

attached to the edge of  $\text{Ti}_4\text{O}_7$  (red dashed line), indicating that the two materials were in close contact with each other, and the theoretical feasibility to construct  $\text{Ti}_3\text{C}_2@\text{Ti}_4\text{O}_7$  was verified in practice. In addition, the intimate contact between the two materials indicated that the heterojunction was successfully established and that there may be interfacial effects between  $\text{Ti}_3\text{C}_2$  MXene and  $\text{Ti}_4\text{O}_7$ . The results of mercury intrusion porosimetry analysis showed that 2%  $\text{Ti}_3\text{C}_2@\text{Ti}_4\text{O}_7$  possessed a smaller median pore diameter (1.37 vs 2.14  $\mu\text{m}$ ) and calculated porosity (52.01% vs 57.49%) compared with those of pristine  $\text{Ti}_4\text{O}_7$  (Fig. S9). The AFM images of 2%  $\text{Ti}_3\text{C}_2@\text{Ti}_4\text{O}_7$  showed larger particles compared with those of pristine  $\text{Ti}_4\text{O}_7$  (Fig. S10).

The Raman spectroscopy results revealed that the D-band and the G-band at 1335 and 1580  $\text{cm}^{-1}$  in pristine  $\text{Ti}_4\text{O}_7$  positively shifted to 1347 and 1587  $\text{cm}^{-1}$  in 2%  $\text{Ti}_3\text{C}_2@\text{Ti}_4\text{O}_7$ , and the absorption intensity ratio  $I_D/I_G$  increased from 1.76 to 1.83 (Fig. S11). The shifts in the peak positions and the increased  $I_D/I_G$  ratio suggested the occurrence of possible strong interfacial interactions and the presence of more defects [40,48], which was consistent with the SEM analyses. The chemical states of the Ti, C, and O elements in 2%  $\text{Ti}_3\text{C}_2@\text{Ti}_4\text{O}_7$  and pristine  $\text{Ti}_4\text{O}_7$  were determined via XPS. The XPS survey spectra are presented in Fig. S12. As shown in Fig. 3j, the two peaks originating from Ti  $2p_{3/2}$  and Ti  $2p_{1/2}$  at 457.6 and 463.4 eV in pristine  $\text{Ti}_4\text{O}_7$  positively shifted to 457.9 and 463.6 eV after doping with  $\text{Ti}_3\text{C}_2$  MXene, respectively. Such positive shifts also occurred in the O 1s spectra, which were deconvoluted into three peaks for 2%  $\text{Ti}_3\text{C}_2@\text{Ti}_4\text{O}_7$  and pristine  $\text{Ti}_4\text{O}_7$  (Fig. 3k). The peaks in the O 1s spectrum of 2%  $\text{Ti}_3\text{C}_2@\text{Ti}_4\text{O}_7$  were ascribed to Ti–O–Ti (529.3 eV), Ti–OH (530.8 eV), and C–OH (532.2 eV), and their

counterparts in the O 1s spectrum of pristine  $\text{Ti}_4\text{O}_7$  were located at 529.1, 530.7, and 532.1 eV, respectively. These upshifts suggested the occurrence of a chemical coupling interaction between  $\text{Ti}_3\text{C}_2$  MXene and  $\text{Ti}_4\text{O}_7$  in the heterostructure [23,49], which was consistent with the newly formed Ti–O–Ti bonds at the interface of the  $\text{Ti}_3\text{C}_2@\text{Ti}_4\text{O}_7$  heterostructure (Fig. 1a). The C 1s spectra of pristine  $\text{Ti}_4\text{O}_7$  and 2%  $\text{Ti}_3\text{C}_2@\text{Ti}_4\text{O}_7$  were fitted by four constituents, namely Ti–C, C–C, C–O, and C=O (Fig. 3l). These four peaks in 2%  $\text{Ti}_3\text{C}_2@\text{Ti}_4\text{O}_7$  were located at 282.2 [46,50], 283.4, 284.5, and 287.0 eV, respectively, while those in pristine  $\text{Ti}_4\text{O}_7$  were located at higher 282.2, 283.5, 284.8, and 287.6 eV, respectively. The positive shifts in the position of the Ti 2p and O 1s peaks and the negative shift in the position of the C 1s peak indicated that the electrons were transferred from  $\text{Ti}_4\text{O}_7$  to  $\text{Ti}_3\text{C}_2$  [51], which is in agreement with the predicted electron flow direction. The shifts in binding energy of the distinct peaks provided strong supporting evidence for interfacial connection at  $\text{Ti}_3\text{C}_2@\text{Ti}_4\text{O}_7$  heterostructure [52]. Compared with pristine  $\text{Ti}_4\text{O}_7$ , the C–O proportion in 2%  $\text{Ti}_3\text{C}_2@\text{Ti}_4\text{O}_7$  increased from 42% to 46%, while the C–C and Ti–C proportions decreased from 49% to 46% and from 4.7% to 2.9%, respectively. These changes possibly resulted from the oxidation reaction during the synthesis of 2%  $\text{Ti}_3\text{C}_2@\text{Ti}_4\text{O}_7$  [46], which may be proved by the theoretical interfacial electron distribution. It could be observed that the electrons were transferred from  $\text{Ti}_4\text{O}_7$  to  $\text{Ti}_3\text{C}_2$  MXene, indicating that the oxidation of  $\text{Ti}_3\text{C}_2$  MXene was caused by the combination of  $\text{Ti}_3\text{C}_2$  MXene and  $\text{Ti}_4\text{O}_7$ , which may also explain the disappearance of the characteristic XRD peak of  $\text{Ti}_3\text{C}_2$  MXene in the XRD pattern of 2%  $\text{Ti}_3\text{C}_2@\text{Ti}_4\text{O}_7$  (Fig. 1b and Fig. S8). Additionally, the experimental WF of



2%  $\text{Ti}_3\text{C}_2@\text{Ti}_4\text{O}_7$  (5.02 eV), pristine  $\text{Ti}_4\text{O}_7$  (4.82 eV), and  $\text{Ti}_3\text{C}_2$  MXene (6.42 eV) (Fig. S13), which were consistent with the theoretical results (4.77 eV for  $\text{Ti}_3\text{C}_2@\text{Ti}_4\text{O}_7$ , 4.67 eV for pristine  $\text{Ti}_4\text{O}_7$ , and 6.60 eV for  $\text{Ti}_3\text{C}_2$  MXene) (Fig. S5).

### 3.3. Electrochemical characterizations, stability, and reactivity of $\text{Ti}_3\text{C}_2@\text{Ti}_4\text{O}_7$

#### 3.3.1. Electrochemical characterizations and stability

According to the EIS tests, the ohmic resistance ( $R_s$ ) values of 2%  $\text{Ti}_3\text{C}_2@\text{Ti}_4\text{O}_7$  and pristine  $\text{Ti}_4\text{O}_7$  were close (4.29 vs 4.71  $\Omega$ ), indicating that the components of EAOP systems (e.g., the electrolyte resistance) provided similar  $R_s$  values (Fig. 4a) [12]. 2%  $\text{Ti}_3\text{C}_2@\text{Ti}_4\text{O}_7$  had a smaller charge-transfer resistance ( $R_{ct}$ ) of 4.21  $\Omega$  than pristine  $\text{Ti}_4\text{O}_7$  ( $R_{ct}$  = 59.09  $\Omega$ ), which is probably ascribed to the numerous oxygen terminals on the surface introduced by  $\text{Ti}_3\text{C}_2$  MXene, which facilitated the increase in the electron transfer rate [53]. The CV plots of 2%  $\text{Ti}_3\text{C}_2@\text{Ti}_4\text{O}_7$  and pristine  $\text{Ti}_4\text{O}_7$  were recorded at potential scan rates varying from 5 to 100 mV/s, and the current increased with the increase in the scan rate (Fig. S14). The voltammetric charge ( $q^*$ ), which is associated with the

specific electroactive sites for charge transfer, as a function of the square root of the scan rate ( $v^{1/2}$ ), was illustrated in Fig. 4b [11]. The slope of the curve of 2%  $\text{Ti}_3\text{C}_2@\text{Ti}_4\text{O}_7$  was 8.02, which was greater than that of pristine  $\text{Ti}_4\text{O}_7$  (3.40) and suggested that 2%  $\text{Ti}_3\text{C}_2@\text{Ti}_4\text{O}_7$  possessed a higher number of electrochemical reactive sites on the surface for electro-oxidation [11]. The integral areas of the CV curves of 2%  $\text{Ti}_3\text{C}_2@\text{Ti}_4\text{O}_7$  were larger by a factor of 2.89 compared with those of pristine  $\text{Ti}_4\text{O}_7$  (Fig. 4b inset). These results demonstrated that doping  $\text{Ti}_4\text{O}_7$  with  $\text{Ti}_3\text{C}_2$  MXene could increase the electroactive area and improve the electrochemical activity owing to the occurrence of interfacial effects between the two constituents [54]. An accelerated service life test was performed to investigate the stability of the two materials at a constant current density of up to 1 A/cm<sup>2</sup>. 2%  $\text{Ti}_3\text{C}_2@\text{Ti}_4\text{O}_7$  exhibited a lifetime of 90.6 h, which was 24% longer than that of pristine  $\text{Ti}_4\text{O}_7$  (73.1 h) (the actual service lifetime calculations were provided in Text S4). The service lifetime of 2%  $\text{Ti}_3\text{C}_2@\text{Ti}_4\text{O}_7$  was 25.9 years and the counterpart of pristine  $\text{Ti}_4\text{O}_7$  was 20.9 years, implying that the presence of  $\text{Ti}_3\text{C}_2$  MXene had an excellent stabilizing effect on the electrode (Fig. 4c). The XPS survey spectrum of 2%  $\text{Ti}_3\text{C}_2@\text{Ti}_4\text{O}_7$  is presented in Fig. S15. The deconvoluted Ti 2p, O 1s, and C 1s XPS spectra show

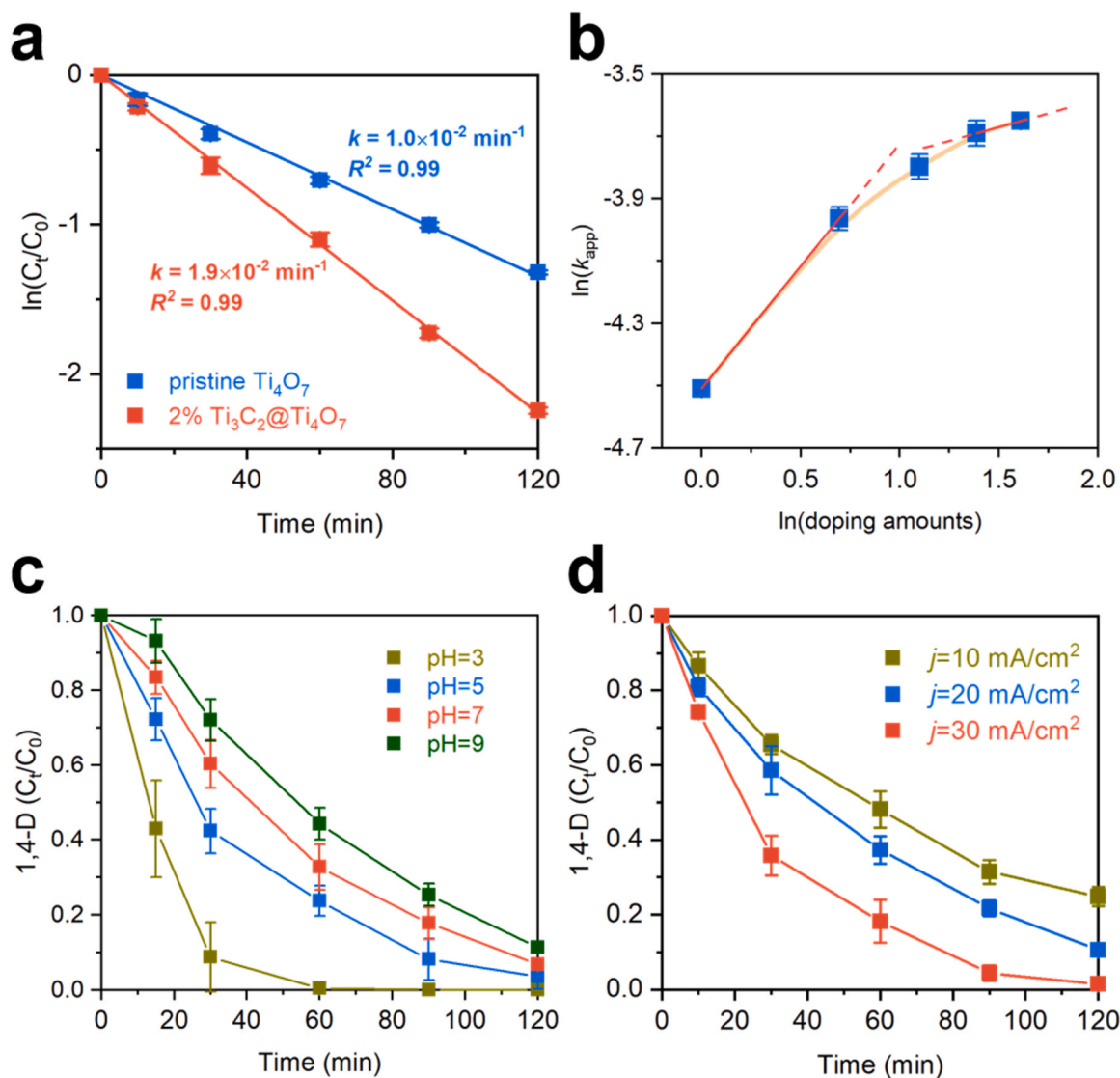


**Fig. 6.** (a) 1,4-D degradation by 2%  $\text{Ti}_3\text{C}_2@\text{Ti}_4\text{O}_7$  and pristine  $\text{Ti}_4\text{O}_7$  and corresponding rate constants. (b) Plot of  $\ln(k_{\text{obs}})$  versus  $\ln(\text{doping amounts})$ ; doping amount (wt%) of  $\text{Ti}_3\text{C}_2$ . Reaction conditions of (a, b):  $[1,4\text{-D}]_0 = 0.1 \text{ mM}$ ,  $j = 20 \text{ mA/cm}^2$ ,  $[\text{Na}_2\text{SO}_4] = 100 \text{ mM}$ . (c, d) Effects of the pH and current density on 1,4-D degradation. Reaction conditions of (c, d):  $[1,4\text{-D}]_0 = 0.1 \text{ mM}$ ,  $[\text{Na}_2\text{SO}_4] = 100 \text{ mM}$ . (e–h) Effects of  $\text{Cl}^-$ ,  $\text{HCO}_3^-$ ,  $\text{H}_2\text{PO}_4^-$ , and  $\text{NO}_3^-$  at different concentrations (0.5–10 mM) on 1,4-D degradation. Reaction conditions of (e–h):  $[1,4\text{-D}]_0 = 0.1 \text{ mM}$ ,  $j = 20 \text{ mA/cm}^2$ ,  $[\text{Na}_2\text{SO}_4] = 100 \text{ mM}$ .

noticeable changes before and after the service life test (Fig. 4d–f). The peak intensities in the Ti 2p and O 1s spectra decreased significantly, especially that corresponding to the Ti–O–Ti bond. Considering the improved electronic properties through the interfacial Ti–O–Ti bond formation, which were both predicted and experimentally verified, the deterioration of the electrode could probably be attributed to the disintegration of the Ti–O–Ti bonds. The increased peak intensity of the C–C bonds after the test may imply the occurrence of a chemical change in the  $\text{Ti}_3\text{C}_2/\text{Ti}_4\text{O}_7$  heterostructure. Cai et al. found that the material obtained by doping  $\text{Ag}_3\text{PO}_4$  with  $\text{Ti}_3\text{C}_2$  MXene could resist corrosion and maintained a high pollutant degradation after eight cycles due to the efficient electron transfer through a Schottky junction [23].  $\text{Ti}_3\text{C}_2$  MXene doping of  $\text{Ti}_4\text{O}_7$  also resulted in the construction of a Schottky junction and the formation of interfacial Ti–O–Ti bonds as demonstrated by the DFT calculations in Sections 3.1.1 and 3.1.2 (Fig. 1c and d); thus, the electron transfer at the interface and the stability of 2%  $\text{Ti}_3\text{C}_2/\text{Ti}_4\text{O}_7$  were greatly enhanced.

### 3.3.2. Electrochemical reactivity

To determine the electrochemical reactivity of 2%  $\text{Ti}_3\text{C}_2/\text{Ti}_4\text{O}_7$  and pristine  $\text{Ti}_4\text{O}_7$ , feasible probes, namely OA, COU, TA, and *p*-BQ, were selected [55]. Prior work proved that OA has a negligible reaction rate with  $\cdot\text{OH}$  ( $k_{\text{OA}}, \cdot\text{OH} = 1.4 \times 10^6 \text{ M}^{-1} \text{ s}^{-1}$ ) [55], and consequently, its degradation can be ascribed to the DET process of the electrodes. The electro-oxidation of 1 mM OA achieved degradations of 50.74% and 22.65% for 2%  $\text{Ti}_3\text{C}_2/\text{Ti}_4\text{O}_7$  and pristine  $\text{Ti}_4\text{O}_7$ , respectively (Fig. 5a). The apparent rate constant ( $k_{\text{app}}$ ) of the OA oxidation ( $k_{\text{OA}}$ ) of 2%  $\text{Ti}_3\text{C}_2/\text{Ti}_4\text{O}_7$  was  $7.6 \times 10^{-3} \text{ min}^{-1}$ , which was 2.62-fold higher than that of  $\text{Ti}_4\text{O}_7$  ( $2.9 \times 10^{-3} \text{ min}^{-1}$ ) (Fig. S16a) (detailed calculations were provided in Text S5). The higher kinetic rate constant implied that doping with  $\text{Ti}_3\text{C}_2$  MXene strengthened the DET process, which was consistent with the lower  $R_{\text{ct}}$  of 2%  $\text{Ti}_3\text{C}_2/\text{Ti}_4\text{O}_7$  (Fig. 4a).

To investigate the  $\cdot\text{OH}$  formation ability of 2%  $\text{Ti}_3\text{C}_2/\text{Ti}_4\text{O}_7$  and pristine  $\text{Ti}_4\text{O}_7$ , COU, TA, and *p*-BQ were used as  $\cdot\text{OH}$  probes. The three probes react with  $\cdot\text{OH}$  at high reaction rates ( $k_{\text{COU}}, \cdot\text{OH} = 2.0 \times 10^9 \text{ M}^{-1} \text{ s}^{-1}$ ,  $k_{\text{TA}}, \cdot\text{OH} = 3.9 \times 10^9 \text{ M}^{-1} \text{ s}^{-1}$ , and  $k_{\text{p-BQ}}, \cdot\text{OH} = 1.2 \times 10^9 \text{ M}^{-1} \text{ s}^{-1}$ ) and generate detectable products, such as 7-hydroxycoumarin (7-HCOU) and 2-hydroxyterephthalic acid (2-HTA), while the disappearance of *p*-BQ was recognized as a signature for  $\cdot\text{OH}$  generation due to the lack of indicative products [56,57]. In Fig. 5b and d, within 90 min, the degradation of COU and TA reached 68.40% and 43.31% for 2%  $\text{Ti}_3\text{C}_2/\text{Ti}_4\text{O}_7$  and 48.80% and 11.13% for pristine  $\text{Ti}_4\text{O}_7$ , respectively. The  $k_{\text{app}}$  values of COU ( $k_{\text{COU}}$ ) and TA ( $k_{\text{TA}}$ ) for 2%  $\text{Ti}_3\text{C}_2/\text{Ti}_4\text{O}_7$  were  $1.4 \times 10^{-2} \text{ min}^{-1}$  and  $6.6 \times 10^{-3} \text{ min}^{-1}$ , respectively, and those for pristine  $\text{Ti}_4\text{O}_7$  were  $7.7 \times 10^{-3} \text{ min}^{-1}$  and  $1.2 \times 10^{-3} \text{ min}^{-1}$ , respectively (Fig. S15b and c; Text S5). Compared with pristine  $\text{Ti}_4\text{O}_7$ , the concentrations of 7-HCOU and 2-HTA produced for 2%  $\text{Ti}_3\text{C}_2/\text{Ti}_4\text{O}_7$  were higher by a factor of 2.29 and 2.57, respectively (Fig. 5b and d). In addition, 90.76% and 72.95% of *p*-BQ, which was used as another  $\cdot\text{OH}$  probe, were removed with 2%  $\text{Ti}_3\text{C}_2/\text{Ti}_4\text{O}_7$  and pristine  $\text{Ti}_4\text{O}_7$ , respectively (Fig. 5c). The above results demonstrated that  $\text{Ti}_3\text{C}_2$  MXene doping was beneficial to increasing the electrochemical reactivity of  $\text{Ti}_4\text{O}_7$ -based composite ceramic membranes, which possibly results from the interface effects between the two materials [54], as well as improving the interfacial charge redistribution of the delocalized electrons, which facilitates electron transfer [27]. Thus, the ROC electro-oxidation ability of 2%  $\text{Ti}_3\text{C}_2/\text{Ti}_4\text{O}_7$  was enhanced. Additionally, the  $\cdot\text{OH}$  formation ability of  $\text{Ti}_3\text{C}_2$  MXene electrode was also determined via  $\cdot\text{OH}$  probes (Text S6 and Fig. S17). Comparing the  $\cdot\text{OH}$  probes degradation results and electrochemical characterizations of 2%  $\text{Ti}_3\text{C}_2/\text{Ti}_4\text{O}_7$  with those of pristine  $\text{Ti}_4\text{O}_7$  and  $\text{Ti}_3\text{C}_2$  MXene electrode, the superiority of  $\text{Ti}_3\text{C}_2$  MXene to serve as a dopant in EAOP electrodes was demonstrated. Specifically, LSV, CV curves, and  $\cdot\text{OH}$  probes degradation of 2%  $\text{Ti}_3\text{C}_2/\text{Ti}_4\text{O}_7$  showed significant improvements in contrast to those in pristine  $\text{Ti}_4\text{O}_7$  (Fig. 4b and Fig. S18). However, the extremely low LSV and CV plots, the tiny amount of  $\cdot\text{OH}$  generation, and

the low 1,4-D decomposition ( $3.8 \pm 0.3\%$  vs  $89.4\% \pm 0.2\%$  in 2%  $\text{Ti}_3\text{C}_2/\text{Ti}_4\text{O}_7$  and  $73.3\% \pm 1.3\%$  in pristine  $\text{Ti}_4\text{O}_7$ ) for  $\text{Ti}_3\text{C}_2$  MXene electrode revealed its weak current density, low oxygen evolution potential, and deficient surface-active sites in electrochemical process (Fig. S17–19). Such huge discrepancy of LSV, CV curves and 1,4-D degradation between  $\text{Ti}_3\text{C}_2$  MXene electrode and 2%  $\text{Ti}_3\text{C}_2/\text{Ti}_4\text{O}_7$ /pristine  $\text{Ti}_4\text{O}_7$  reflected the critical role of  $\text{Ti}_3\text{C}_2$  MXene in modifying EAOP electrodes. The improved electron migration and enhanced catalytic performance in 2%  $\text{Ti}_3\text{C}_2/\text{Ti}_4\text{O}_7$  was attributed to the interface effect at 2%  $\text{Ti}_3\text{C}_2/\text{Ti}_4\text{O}_7$  heterostructure.

### 3.4. Electro-oxidation of 1,4-D by $\text{Ti}_3\text{C}_2/\text{Ti}_4\text{O}_7$

#### 3.4.1. Degradation of 1,4-D by $\text{Ti}_3\text{C}_2/\text{Ti}_4\text{O}_7$

At an applied constant current of  $20 \text{ mA/cm}^2$  (working potential =  $3.36 \text{ V}$  vs  $\text{Ag/AgCl}$  (Fig. S20)), 2%  $\text{Ti}_3\text{C}_2/\text{Ti}_4\text{O}_7$  achieved a 1,4-D degradation efficiency of  $89.4\% \pm 0.2\%$  after treatment for 120 min, which corresponded to an improvement of 22% with respect to pristine  $\text{Ti}_4\text{O}_7$  ( $73.3\% \pm 1.3\%$ ) (Fig. S21). The degradation of 1,4-D was in good agreement for both materials with the pseudo-first-order kinetic reaction model when assuming that the  $\cdot\text{OH}$  concentration was in a quasi-stationary state [7]. The  $k_{\text{app}}$  of 1,4-D for 2%  $\text{Ti}_3\text{C}_2/\text{Ti}_4\text{O}_7$  ( $k_{\text{Ti}_3\text{C}_2/\text{Ti}_4\text{O}_7} = 1.9 \times 10^{-2} \text{ min}^{-1}$ ) was 1.9-fold higher than that of pristine  $\text{Ti}_4\text{O}_7$  ( $k_{\text{pristine Ti}_4\text{O}_7} = 1.0 \times 10^{-2} \text{ min}^{-1}$ ) (Fig. 6a; Text S5). The above results confirmed that 2%  $\text{Ti}_3\text{C}_2/\text{Ti}_4\text{O}_7$  possessed faster oxidation kinetics and better performance to eliminate 1,4-D compared with pristine  $\text{Ti}_4\text{O}_7$ . The XPS spectra of used 2%  $\text{Ti}_3\text{C}_2/\text{Ti}_4\text{O}_7$  were conducted to investigate the chemical states changes of elements. It could be found that the survey spectra and the vast majority of Ti, C, and O deconvolution results of used 2%  $\text{Ti}_3\text{C}_2/\text{Ti}_4\text{O}_7$  were quite similar to those in fresh electrode (Fig. S22 and S23), with a C–OH ratio in C 1s spectrum decreased from 15.1% to 9.2% in 2%  $\text{Ti}_3\text{C}_2/\text{Ti}_4\text{O}_7$  (Fig. S23). Furthermore, CV and EIS curves of used 2%  $\text{Ti}_3\text{C}_2/\text{Ti}_4\text{O}_7$  also displayed similar graphs to those of fresh electrode (Fig. S24). These results corresponded well with the stable performances of 2%  $\text{Ti}_3\text{C}_2/\text{Ti}_4\text{O}_7$  within their lifespans reflecting in the accelerated service lifetime test.

In situ electron paramagnetic resonance results clearly showed the characteristic 1:2:2:1 quadruple signal of  $\text{DMPO} \cdot \text{OH}$  ( $\alpha_{\text{N}} = \alpha_{\text{H}} = 14.9 \text{ G}$ ), which indicated the presence of  $\cdot\text{OH}$  in the EAOP system [58] (Text S7; Fig. S25). Quenching experiments demonstrated that  $36.0\% \pm 1.3\%$  of 1,4-D could still be degraded even with three orders of magnitude higher concentrations of the radical scavenger MeOH than that of 1,4-D. These results indicated that the DET process significantly contributed to 1,4-D degradation (Text S8; Fig. S26). Thus, the removal of 1,4-D greatly improved due to the enhanced DET process and increased  $\cdot\text{OH}$  generation.

The 1,4-D electro-oxidation mediated by  $\text{Ti}_3\text{C}_2/\text{Ti}_4\text{O}_7$  was conducted at different  $\text{Ti}_3\text{C}_2$  MXene doping amounts ( $X\% = 1\text{--}5 \text{ wt}\%$ ) to optimize the amount of the dopant. Using these  $X\%$   $\text{Ti}_3\text{C}_2/\text{Ti}_4\text{O}_7$  electrodes, the  $\ln(k_{\text{app}})$  values of 1,4-D degradation were plotted as a function of  $\ln(\text{doping amounts})$  (Fig. 6b). With increasing doping amounts, the slopes decreased gradually from 0.78 to 0.26, indicating that an increase in the doping amount was beneficial to 1,4-D decomposition, although it was not sufficiently cost-effective.

The influences of other parameters, such as the pH (3, 5, 7, and 9) and current densities (ranging from 10 to  $30 \text{ mA/cm}^2$ ) on the decomposition of 1,4-D by 2%  $\text{Ti}_3\text{C}_2/\text{Ti}_4\text{O}_7$  were also explored. A notable pH effect on 1,4-D degradation was observed; complete removal was reached within 60 min at  $\text{pH} = 3$ , while 1,4-D was still present at a higher pH after 120 min (Fig. 6c). The enhanced 1,4-D degradation in acidic conditions was possibly ascribed to the stronger oxidation reactivity of  $\cdot\text{OH}$  than those in neutral or alkaline conditions [59]. In addition to the weaker oxidation ability of  $\cdot\text{OH}$  at a higher pH, the decrease in 1,4-D decomposition with increasing pH is also ascribed to insufficient  $\cdot\text{OH}$  generation. A higher pH implied a higher  $\text{OH}^-$  concentration, promoting the transfer of more electrons from  $\text{OH}^-$  on the anode surface

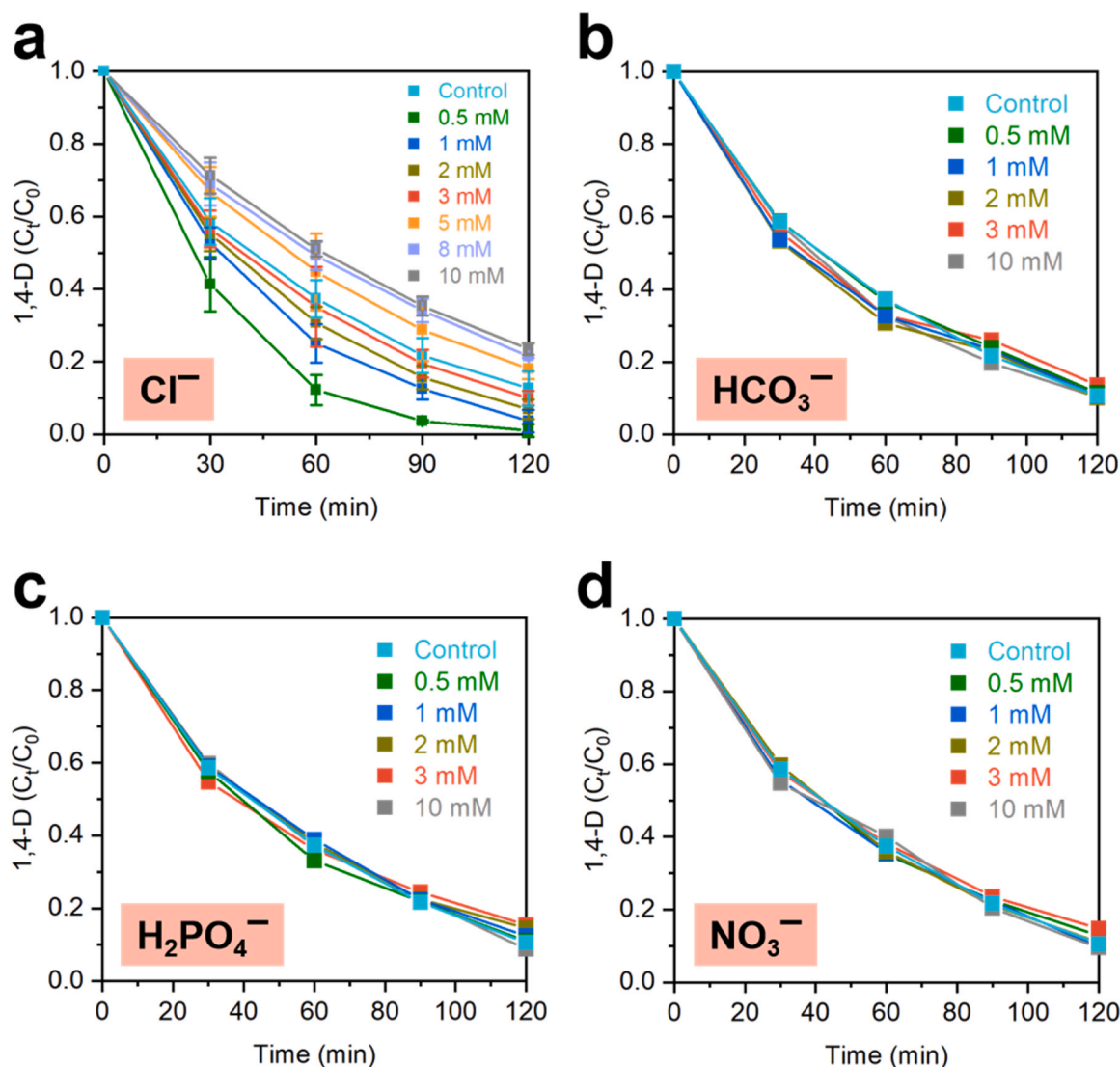


**Fig. 7.** (a–d) Effects of  $Cl^-$ ,  $HCO_3^-$ ,  $H_2PO_4^-$ , and  $NO_3^-$  at different concentrations (0.5–10 mM) on 1,4-D degradation. Reaction conditions of (e–h):  $[1,4-D]_0 = 0.1$  mM,  $j = 20$  mA/cm<sup>2</sup>,  $[Na_2SO_4] = 100$  mM.

and finally facilitating oxygen production according to the oxygen evolution reaction (OER) mechanism (Text S9) [60,61]. The enhanced OER would inevitably compete with the  $\cdot OH$  formation reaction, resulting in a decrease in  $\cdot OH$  generation. In addition, the 1,4-D removal increased from  $75.2\% \pm 2.5$  to  $98.9\% \pm 0.6\%$  as the current density increased from 10 to 30 mA/cm<sup>2</sup> (Fig. 6d). These investigations showed that acidic conditions and high current densities improved 1,4-D degradation, which may increase capital cost and energy consumption.

### 3.4.2. Degradation performance in different water matrices

To evaluate the feasibility of 1,4-D removal via 2%  $Ti_3C_2@Ti_4O_7$  in water matrices containing different ions, the effects of selected anions present at various concentrations, i.e.,  $Cl^-$ ,  $HCO_3^-$ ,  $H_2PO_4^-$ , and  $NO_3^-$ , on the degradation of 1,4-D were explored. It is noteworthy that different concentrations of  $Cl^-$  led to contradicting results for 1,4-D decomposition (Fig. 7a). While a  $Cl^-$  concentration in the range of 0.5–3 mM was found to be beneficial for the decomposition of 1,4-D, concentrations in the range of 5–10 mM resulted in a reduced 1,4-D degradation. The enhanced 1,4-D removal at lower  $Cl^-$  concentrations can be attributed to the generation of  $Cl^\bullet$  and  $Cl_2^\bullet$  (detailed equations could be found in Text S10) [62,63]. However, the contribution of these reactions to 1,4-D removal declined with increasing  $Cl^-$  concentration (Fig. 7a), and

compared with the control experiment, the 1,4-D degradation decreased when  $Cl^-$  concentrations was above 3 mM. These results are probably caused by the occupation of the active sites of 2%  $Ti_3C_2@Ti_4O_7$  by excessive  $Cl^-$ , which would be rapidly transformed by  $\cdot OH$  into  $Cl_2^\bullet$ ; not only is this radical less reactive than  $\cdot OH$ , but this reaction pathway also results in a decrease in  $\cdot OH$  concentration (Text S10) [64]. The large amount of  $Cl_2^\bullet$  and the reduced amount of  $\cdot OH$  resulted in the inhibition of 1,4-D degradation. By contrast, the presence of  $HCO_3^-$ ,  $H_2PO_4^-$ , or  $NO_3^-$  did not show any significant influence on 1,4-D decomposition (Fig. 7b–d).

### 3.5. Application of 1,4-D removal by $Ti_3C_2@Ti_4O_7$

To further assess the application feasibility of 2%  $Ti_3C_2@Ti_4O_7$  for the removal of 1,4-D, the formation of chlorinated byproducts (using simulated water spiked with 1 mM  $Cl^-$ ) at different current densities, 1,4-D degradation in real groundwater, and normalized electric energy (EE/O, kWh/m<sup>3</sup>) per log removal of 1,4-D were investigated (Texts S11 and S12).  $Cl^-$  could be oxidized to  $ClO_3^-$  and  $ClO_4^-$  at the anode surface, and since these inorganic chlorinated byproducts were reported to cause health risks [9], their generation should be monitored. It was found that the production of  $ClO_3^-$  and  $ClO_4^-$  increased from 24.1 to 203.4  $\mu M$



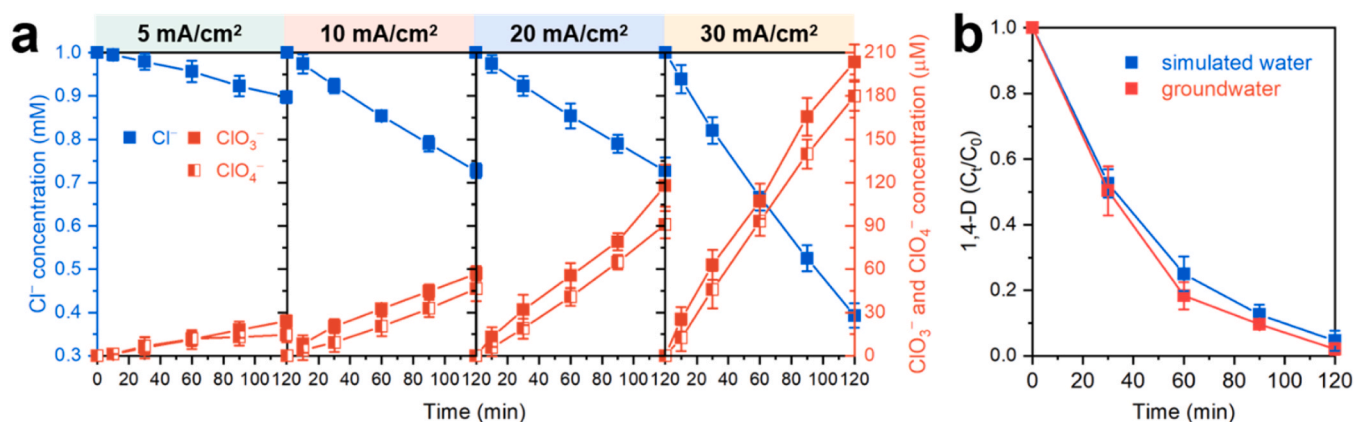


**Fig. 8.** (a)  $\text{Cl}^-$  degradation and the generation of chlorinated byproducts at different current densities (5–30  $\text{mA}/\text{cm}^2$ ). Reaction conditions:  $j = 20 \text{ mA}/\text{cm}^2$ ,  $[\text{Na}_2\text{SO}_4] = 100 \text{ mM}$ . (b) 1,4-D degradation in simulated water and natural groundwater. Reaction conditions:  $[1,4\text{-D}]_0 = 0.1 \text{ mM}$ ,  $j = 20 \text{ mA}/\text{cm}^2$ ,  $[\text{Na}_2\text{SO}_4] = 100 \text{ mM}$ .

( $\text{ClO}_3^-$ ) and from 14.5 to 179.8  $\mu\text{M}$  ( $\text{ClO}_4^-$ ) when the applied current was raised from 5 to 30  $\text{mA}/\text{cm}^2$  (Fig. 8a). The increase in  $\text{ClO}_3^-$  and  $\text{ClO}_4^-$  production possibly resulted from the enhanced  $\cdot\text{OH}$  generation at higher current densities, indicating that the application of 2%  $\text{Ti}_3\text{C}_2@-\text{Ti}_4\text{O}_7$  for 1,4-D removal required the application of an optimized current to limit the formation of these chlorinated byproducts. Furthermore, we investigated the 1,4-D degradation performance in real groundwater containing 27.7  $\text{mg}/\text{L}$   $\text{Cl}^-$ . The 1,4-D decomposition performance in both real groundwater and simulated water was excellent, and the residual 1,4-D concentrations were below 4  $\mu\text{M}$  (3.7  $\mu\text{M}$  in simulated water and 2.1  $\mu\text{M}$  in groundwater) (Fig. 8b), which met the requirements for drinking water [11]. In addition, the energy consumption during 1,4-D removal was evaluated. The EE/O for 2%  $\text{Ti}_3\text{C}_2@-\text{Ti}_4\text{O}_7$  reached 10.3  $\text{kWh}/\text{m}^3$  throughout the 1,4-D degradation process, while that in pristine  $\text{Ti}_4\text{O}_7$  was 2.2-fold higher (22.6  $\text{kWh}/\text{m}^3$ ). Compared to pristine  $\text{Ti}_4\text{O}_7$ , 2%  $\text{Ti}_3\text{C}_2@-\text{Ti}_4\text{O}_7$  can be anticipated to be a promising EAOP anode for 1,4-D removal due to its superior removal efficiency and high cost-effectiveness.

#### 4. Conclusions

This study demonstrated through theoretical predictions the feasibility and superiority of  $\text{Ti}_3\text{C}_2$  MXene to serve as a highly effective electrocatalyst and provided insights into the  $\text{Ti}_3\text{C}_2@-\text{Ti}_4\text{O}_7$  heterostructure and its  $\cdot\text{OH}$  generation mechanism. The newly formed interfacial Ti–O–Ti bond was considered to be associated with the enhanced chemical stability, electron transfer, and electrochemical reactivity. The  $\cdot\text{OH}$  generation of  $\text{Ti}_3\text{C}_2@-\text{Ti}_4\text{O}_7$  was greatly improved compared with that of pristine  $\text{Ti}_4\text{O}_7$  due to the lower reaction energies of  $\text{H}_2\text{O}$  adsorption, OH group transformation, and  $\cdot\text{OH}$  desorption. 2%  $\text{Ti}_3\text{C}_2@-\text{Ti}_4\text{O}_7$  performed excellently in 1,4-D removal, and the residual 1,4-D concentration in real groundwater met the requirements for drinking water. This work combined theoretical calculations with experiments to demonstrate the feasibility of employing an interface engineering strategy for  $\text{Ti}_4\text{O}_7$  electrodes by doping them with  $\text{Ti}_3\text{C}_2$  MXene to achieve an improved EAOP performance. However, improving the mass transfer between ROC and this novel anode in EAOP remains challenging. Due to its advantageous pore size (1.37  $\mu\text{m}$ ), 2%  $\text{Ti}_3\text{C}_2@-\text{Ti}_4\text{O}_7$  can be anticipated to be used in EAOPs with a flow-through membrane to increase the mass transfer and lower the energy consumption in future research to meet the requirements for practical applications.

#### CRediT authorship contribution statement

**Kuanchang He:** Methodology, Investigation, Data Curation, Formal

analysis, Validation, Writing-Original Draft. **Wei Li:** Conceptualization, Investigation, Methodology, Formal analysis, Data Curation, Funding acquisition, Writing-Original Draft, Writing-Review&Editing, Supervision. **Longxiang Tang:** Data Curation, Methodology, Investigation. **Lingyu Chen:** Data Curation, Formal analysis. **Gang Wang:** Methodology, Visualization. **Qian Liu:** Investigation, Data Curation. **Xiaodong Xin:** Resources, Investigation. **Cao Yang:** Formal analysis. **Zhenbei Wang:** Data Curation. **Sihaio Lv:** Supervision. **Defeng Xing:** Supervision, Resources, Funding acquisition, Writing-Review&Editing.

#### Declaration of Competing Interest

The authors declare that they have no known competing financial interests or personal relationships that could have appeared to influence the work reported in this paper.

#### Data availability

No data was used for the research described in the article.

#### Acknowledgements

This study was supported by National Natural Science Foundation of China [U22A20443, 52000026], Guangdong Basic and Applied Basic Research Foundation [2022A1515140015], Characteristic Innovation Project of Guangdong Universities [2022KTSX139], and the Interdisciplinary Research Foundation of HIT and National Key Research and Development Program [2022YFA0912503]. The authors are also especially thankful to Ms. Xue Bai for assistance with graphic abstract design.

#### Appendix A. Supporting information

Supplementary data associated with this article can be found in the online version at [doi:10.1016/j.apcatb.2023.123077](https://doi.org/10.1016/j.apcatb.2023.123077).

#### References

- [1] W. Li, S. Patton, J.M. Gleason, S.P. Mezyk, K.P. Ishida, H. Liu, UV photolysis of chloramine and persulfate for 1,4-dioxane removal in reverse-osmosis permeate for potable water reuse, *Environ. Sci. Technol.* 52 (2018) 6417–6425, <https://doi.org/10.1021/acs.est.7b06042>.
- [2] S. Patton, M. Romano, V. Naddeo, K.P. Ishida, H. Liu, Photolysis of mono- and dichloramines in UV/hydrogen peroxide: Effects on 1,4-dioxane removal and relevance in water reuse, *Environ. Sci. Technol.* 52 (2018) 11720–11727, <https://doi.org/10.1021/acs.est.8b01023>.
- [3] M. Sun, C. Lopez-Velandia, D.R. Knappe, Determination of 1,4-dioxane in the cape fear river watershed by heated purge-and-trap preconcentration and gas chromatography-mass spectrometry, *Environ. Sci. Technol.* 50 (2016) 2246–2254, <https://doi.org/10.1021/acs.est.5b05875>.

- [4] B.C. Hodges, E.L. Cates, J.H. Kim, Challenges and prospects of advanced oxidation water treatment processes using catalytic nanomaterials, *Nat. Nanotechnol.* 13 (2018) 642–650, <https://doi.org/10.1038/s41565-018-0216-x>.
- [5] B.P. Chaplin, G. Schrader, J. Farrell, Electrochemical destruction of N-nitrosodimethylamine in reverse osmosis concentrates using Boron-doped diamond film electrodes, *Environ. Sci. Technol.* 44 (2010) 4264–4269, <https://doi.org/10.1021/es903872p>.
- [6] B.P. Chaplin, The prospect of electrochemical technologies advancing worldwide water treatment, *Acc. Chem. Res.* 52 (2019) 596–604, <https://doi.org/10.1021/acs.accounts.8b00611>.
- [7] S.O. Ganiyu, N. Oturan, S. Raffy, M. Cretin, R. Esmilaire, E. van Hullebusch, G. Esposito, M.A. Oturan, Sub-stoichiometric titanium oxide ( $\text{Ti}_4\text{O}_7$ ) as a suitable ceramic anode for electrooxidation of organic pollutants: A case study of kinetics, mineralization and toxicity assessment of amoxicillin, *Water Res.* 106 (2016) 171–182, <https://doi.org/10.1016/j.watres.2016.09.056>.
- [8] F.C. Moreira, R.A.R. Boaventura, E. Brillas, V.J.P. Vilar, Electrochemical advanced oxidation processes: A review on their application to synthetic and real wastewaters, *Appl. Catal. B Environ.* 202 (2017) 217–261, <https://doi.org/10.1016/j.apcatb.2016.08.037>.
- [9] M.H. Lin, D.M. Bulman, C.K. Remucal, B.P. Chaplin, Chlorinated byproduct formation during the electrochemical advanced oxidation process at Magnéli phase  $\text{Ti}_4\text{O}_7$  electrodes, *Environ. Sci. Technol.* 54 (2020) 12673–12683, <https://doi.org/10.1021/acs.est.0c03916>.
- [10] J. Xie, J. Ma, C. Zhang, T.D. Waite, Direct electron transfer (DET) processes in a flow anode system-energy-efficient electrochemical oxidation of phenol, *Water Res.* 203 (2021), 117547, <https://doi.org/10.1016/j.watres.2021.117547>.
- [11] W. Li, R. Xiao, J. Xu, H. Lin, K. Yang, W. Li, K. He, L. Tang, J. Chen, Y. Wu, S. Lv, Interface engineering strategy of a  $\text{Ti}_4\text{O}_7$  ceramic membrane via graphene oxide nanoparticles toward efficient electrooxidation of 1,4-dioxane, *Water Res.* 216 (2022), 118287, <https://doi.org/10.1016/j.watres.2022.118287>.
- [12] H. Lin, R. Xiao, R. Xie, L. Yang, C. Tang, R. Wang, J. Chen, S. Lv, Q. Huang, Defect engineering on a  $\text{Ti}_4\text{O}_7$  electrode by  $\text{Ce}^{3+}$  doping for the efficient electrooxidation of perfluorooctanesulfonate, *Environ. Sci. Technol.* 55 (2021) 2597–2607, <https://doi.org/10.1021/acs.est.0c06881>.
- [13] J. Xie, J. Ma, C. Zhang, X. Kong, Z. Wang, T.D. Waite, Effect of the presence of carbon in  $\text{Ti}_4\text{O}_7$  electrodes on anodic oxidation of contaminants, *Environ. Sci. Technol.* 54 (2020) 5227–5236, <https://doi.org/10.1021/acs.est.9b07398>.
- [14] X. Du, M.A. Oturan, M. Zhou, N. Belkessa, P. Su, J. Cai, C. Trellu, E. Mousset, Nanostructured electrodes for electrocatalytic advanced oxidation processes: From materials preparation to mechanisms understanding and wastewater treatment applications, *Appl. Catal. B Environ.* 296 (2021), 120332, <https://doi.org/10.1016/j.apcatb.2021.120332>.
- [15] M. El Kateb, C. Trellu, A. Darwich, M. Rivallin, M. Bechelany, S. Nagarajan, S. Lacour, N. Bellakhal, G. Lesage, M. Heran, M. Cretin, Electrochemical advanced oxidation processes using novel electrode materials for mineralization and biodegradability enhancement of nanofiltration concentrate of landfill leachates, *Water Res.* 162 (2019) 446–455, <https://doi.org/10.1016/j.watres.2019.07.005>.
- [16] S.O. Ganiyu, N. Oturan, S. Raffy, G. Esposito, E.D. van Hullebusch, M. Cretin, M. A. Oturan, Use of sub-stoichiometric titanium oxide as a ceramic electrode in anodic oxidation and electrofenton degradation of the beta-blocker propranolol: Degradation kinetics and mineralization pathway, *Electrochim. Acta* 242 (2017) 344–354, <https://doi.org/10.1016/j.electacta.2017.05.047>.
- [17] S. Nayak, B.P. Chaplin, Fabrication and characterization of porous, conductive, monolithic  $\text{Ti}_4\text{O}_7$  electrodes, *Electrochim. Acta* 263 (2018) 299–310, <https://doi.org/10.1016/j.electacta.2018.01.034>.
- [18] L. Ding, L. Li, Y. Liu, Y. Wu, Z. Lu, J. Deng, Y. Wei, J. Caro, H. Wang, Effective ion sieving with  $\text{Ti}_3\text{C}_2\text{X}$  MXene membranes for production of drinking water from seawater, *Nat. Sustain.* 3 (2020) 296–302, <https://doi.org/10.1038/s41893-020-0474-0>.
- [19] S. Wang, Z. Li, G. Wang, Y. Wang, Z. Ling, C. Li, Freestanding  $\text{Ti}_3\text{C}_2\text{X}$  MXene/prussian blue analogues films with superior ion uptake for efficient capacitive deionization by a dual pseudocapacitance effect, *ACS Nano* 16 (2022) 1239–1249, <https://doi.org/10.1021/acsnano.1c09036>.
- [20] Y. Wang, T. Guo, Z. Tian, K. Bibi, Y.Z. Zhang, H.N. Alshareef, MXenes for energy harvesting, *Adv. Mater.* (2022), e2108560, <https://doi.org/10.1002/adma.202108560>.
- [21] M. Ghidui, M.R. Lukatskaya, M.Q. Zhao, Y. Gogotsi, M.W. Barsoum, Conductive two-dimensional titanium carbide 'clay' with high volumetric capacitance, *Nature* 516 (2014) 78–81, <https://doi.org/10.1038/nature13970>.
- [22] Y. Li, J. Ma, T.D. Waite, M.R. Hoffmann, Z. Wang, Development of a mechanically flexible 2D-MXene membrane cathode for selective electrochemical reduction of nitrate to  $\text{N}_2$ : Mechanisms and implications, *Environ. Sci. Technol.* 55 (2021) 10695–10703, <https://doi.org/10.1021/acs.est.1c00264>.
- [23] T. Cai, L. Wang, Y. Liu, S. Zhang, W. Dong, H. Chen, X. Yi, J. Yuan, X. Xia, C. Liu, S. Luo,  $\text{Ag}_3\text{PO}_4/\text{Ti}_3\text{C}_2$  MXene interface materials as a Schottky catalyst with enhanced photocatalytic activities and anti-photocorrosion performance, *Appl. Catal. B Environ.* 239 (2018) 545–554, <https://doi.org/10.1016/j.apcatb.2018.08.053>.
- [24] S.J. Clark, M.D. Segall, C.J. Pickard, P.J. Hasnip, M.I.J. Probert, K. Refson, M. C. Payne, First principles methods using CASTEP, *Z. Krist. Cryst. Mater.* 220 (2005) 567–570, <https://doi.org/10.1524/zkri.220.5.567.65075>.
- [25] J.P. Perdew, K. Burke, M. Ernzerhof, Generalized gradient approximation made simple, *Phys. Rev. Lett.* 77 (1996) 3865–3868, <https://doi.org/10.1103/PhysRevLett.77.3865>.
- [26] M. Li, Y.T. Jin, J.F. Yan, Z. Liu, N.X. Feng, W. Han, L.W. Huang, Q.K. Li, K.L. Yeung, S.Q. Zhou, C.H. Mo, Exploration of perfluorooctane sulfonate degradation properties and mechanism via electron-transfer dominated radical process, *Water Res.* 215 (2022), 118259, <https://doi.org/10.1016/j.watres.2022.118259>.
- [27] L. Liu, Q. Zhao, R. Liu, L. Zhu, Hydrogen adsorption-induced catalytic enhancement over Cu nanoparticles immobilized by layered  $\text{Ti}_3\text{C}_2$  MXene, *Appl. Catal. B Environ.* 252 (2019) 198–204, <https://doi.org/10.1016/j.apcatb.2019.04.026>.
- [28] R. Zhang, X. Huang, D. Wang, T.K.A. Hoang, Y. Yang, X. Duan, P. Chen, L.-C. Qin, G. Wen, Single-phase mixed transition metal carbonate encapsulated by graphene: Facile synthesis and improved lithium storage properties, *Adv. Funct. Mater.* 28 (2018) 1705817, <https://doi.org/10.1002/adfm.201705817>.
- [29] J. Zhou, D. Li, W. Zhao, B. Jing, Z. Ao, T. An, First-principles evaluation of volatile organic compounds degradation in Z-scheme photocatalytic systems: MXene and graphitic-CN heterostructures, *ACS Appl. Mater. Inter.* 13 (2021) 23843–23852, <https://doi.org/10.1021/acsami.1c05617>.
- [30] B. Zhang, Y. Chang, Y. Wu, Z. Fan, P. Zhai, C. Wang, J. Gao, L. Sun, J. Hou, Regulating  $^{\circ}\text{CHO}$  intermediate as rate-determining step of defective oxynitride nanosheets enabling robust  $\text{CO}_2$  electroreduction, *Adv. Energy Mater.* 12 (2022) 2200321, <https://doi.org/10.1002/aenm.202200321>.
- [31] Y. Sun, D. Jin, Y. Sun, X. Meng, Y. Gao, Y. Dall'Agnese, G. Chen, X.-F. Wang, g- $\text{C}_3\text{N}_4/\text{Ti}_3\text{C}_2\text{Tx}$  (MXenes) composite with oxidized surface groups for efficient photocatalytic hydrogen evolution, *J. Mater. Chem. A* 6 (2018) 9124–9131, <https://doi.org/10.1039/c8ta02706d>.
- [32] J. Ran, G. Gao, F.T. Li, T.Y. Ma, A. Du, S.Z. Qiao,  $\text{Ti}_3\text{C}_2$  MXene co-catalyst on metal sulfide photo-absorbers for enhanced visible-light photocatalytic hydrogen production, *Nat. Commun.* 8 (2017) 13907, <https://doi.org/10.1038/ncomms13907>.
- [33] S. Garcia-Segura, X. Qu, P.J.J. Alvarez, B.P. Chaplin, W. Chen, J.C. Crittenden, Y. Feng, G. Gao, Z. He, C.-H. Hou, X. Hu, G. Jiang, J.-H. Kim, J. Li, Q. Li, J. Ma, J. Ma, A.B. Nienhauser, J. Niu, B. Pan, X. Quan, F. Ronzani, D. Villagran, T. D. Waite, W.S. Walker, C. Wang, M.S. Wong, P. Westerhoff, Opportunities for nanotechnology to enhance electrochemical treatment of pollutants in potable water and industrial wastewater – a perspective, *Environ. Sci. Nano* 7 (2020) 2178–2194, <https://doi.org/10.1039/d0en00194e>.
- [34] A. Liu, X. Liang, X. Ren, W. Guan, M. Gao, Y. Yang, Q. Yang, L. Gao, Y. Li, T. Ma, Recent progress in MXene-based materials: Potential high-performance electrocatalysts, *Adv. Funct. Mater.* 30 (2020) 2003437, <https://doi.org/10.1002/adfm.202003437>.
- [35] J. Li, Z. Li, X. Liu, C. Li, Y. Zheng, K.W.K. Yeung, Z. Cui, Y. Liang, S. Zhu, W. Hu, Y. Qi, T. Zhang, X. Wang, S. Wu, Interfacial engineering of  $\text{Bi}_2\text{S}_3/\text{Ti}_3\text{C}_2\text{Tx}$  MXene based on work function for rapid photo-excited bacteria-killing, *Nat. Commun.* 12 (2021) 1224, <https://doi.org/10.1038/s41467-021-21435-6>.
- [36] X. Wu, Y. Wang, Z.-S. Wu, Design principle of electrocatalysts for the electrooxidation of organics, *Chem* 8 (2022) 1–36, <https://doi.org/10.1016/j.chempr.2022.07.010>.
- [37] L. Tao, D. Dastan, W. Wang, P. Poldorn, X. Meng, M. Wu, H. Zhao, H. Zhang, L. Li, B. An, Metal-decorated  $\text{InN}$  monolayer senses  $\text{N}_2$  against  $\text{CO}_2$ , *ACS Appl. Mater. Interfaces* 15 (2023) 12534–12544, <https://doi.org/10.1021/acsaami.2c21463>.
- [38] Y. Wang, X. Li, M. Zhang, Y. Zhou, D. Rao, C. Zhong, J. Zhang, X. Han, W. Hu, Y. Zhang, K. Zaghib, Y. Wang, Y. Deng, Lattice-strain engineering of homogeneous  $\text{NiSe}_0.5\text{Se}_{0.5}$  core-shell nanostructure as a highly efficient and robust electrocatalyst for overall water splitting, *Adv. Mater.* 32 (2020), e2000231, <https://doi.org/10.1002/adma.202000231>.
- [39] Y. Pan, K. Sun, Y. Lin, X. Cao, Y. Cheng, S. Liu, L. Zeng, W.-C. Cheong, D. Zhao, K. Wu, Z. Liu, Y. Liu, D. Wang, Q. Peng, C. Chen, Y. Li, Electronic structure and d-band center control engineering over M-doped  $\text{CoP}$  ( $\text{M} = \text{Ni}, \text{Mn}, \text{Fe}$ ) hollow polyhedron frames for boosting hydrogen production, *Nano Energy* 56 (2019) 411–419, <https://doi.org/10.1016/j.nanoen.2018.11.034>.
- [40] Z. Lv, W. Ma, M. Wang, J. Dang, K. Jian, D. Liu, D. Huang, Co-constructing interfaces of multiheterostructure on MXene ( $\text{Ti}_3\text{C}_2\text{Tx}$ )-modified 3D self-supporting electrode for ultraefficient electrocatalytic HER in alkaline media, *Adv. Funct. Mater.* 31 (2021) 2102576, <https://doi.org/10.1002/adfm.202102576>.
- [41] Z. Chen, Y. Song, J. Cai, X. Zheng, D. Han, Y. Wu, Y. Zang, S. Niu, Y. Liu, J. Zhu, X. Liu, G. Wang, Tailoring the d-band centers enables  $\text{Co}_4\text{N}$  nanosheets to be highly active for hydrogen evolution catalysis, *Angew. Chem. Int. Ed. Engl.* 130 (2018) 5170–5174, <https://doi.org/10.1002/ange.201801834>.
- [42] L. Li, Y. Wang, Q. Huang, First-principles study of the degradation of perfluorooctanesulfonate and perfluorobutanesulfonate on a Magnéli Phase  $\text{Ti}_4\text{O}_7$  anode, *ACS ES&T Water* 1 (2021) 1737–1744, <https://doi.org/10.1021/acsestwater.1c00086>.
- [43] D. He, X. Song, W. Li, C. Tang, J. Liu, Z. Ke, C. Jiang, X. Xiao, Active electron density modulation of  $\text{Co}_3\text{O}_4$ -based catalysts enhances their oxygen evolution performance, *Angew. Chem. Int. Ed. Engl.* 59 (2020) 6929–6935, <https://doi.org/10.1002/anie.202001681>.
- [44] L. Ma, L.-J. Yu, J. Liu, Y.-Q. Su, S. Li, X. Zhang, T. Meng, S. Zhang, J. Song, J. Wang, X. Zhao, Z. Cui, N. Wang, Y. Zhao, Construction of  $\text{Ti}_4\text{O}_7/\text{TiN}$ /carbon microdisk sulfur host with strong polar N–Ti–O bond for ultralong life lithium–sulfur battery, *Energy Storage Mater.* 44 (2022) 180–189, <https://doi.org/10.1016/j.ensm.2021.09.024>.
- [45] Y. Zhang, L. Tao, C. Xie, D. Wang, Y. Zou, R. Chen, Y. Wang, C. Jia, S. Wang, Defect engineering on electrode materials for rechargeable batteries, *Adv. Mater.* 32 (2020), e1905923, <https://doi.org/10.1002/adma.201905923>.
- [46] B. Wang, M. Wang, F. Liu, Q. Zhang, S. Yao, X. Liu, F. Huang,  $\text{Ti}_3\text{C}_2$ : An ideal co-catalyst? *Angew. Chem. Int. Ed. Engl.* 59 (2020) 1914–1918, <https://doi.org/10.1002/anie.201913095>.
- [47] H. Shi, P. Zhang, Z. Liu, S. Park, M.R. Lohe, Y. Wu, A. Shaygan Nia, S. Yang, X. Feng, Ambient-stable two-dimensional titanium carbide (MXene) enabled by

- Iodine etching, *Angew. Chem. Int. Ed. Engl.* 60 (2021) 8689–8693, <https://doi.org/10.1002/anie.202015627>.
- [48] C. Yang, Y. Tang, Y. Tian, Y. Luo, M. Faraz Ud Din, X. Yin, W. Que, Flexible nitrogen-doped 2D titanium carbides (MXene) films constructed by an ex situ solvothermal method with extraordinary volumetric capacitance, *Adv. Energy Mater.* 8 (2018) 1802087, <https://doi.org/10.1002/aenm.201802087>.
- [49] K.B. Ibrahim, W.-N. Su, M.-C. Tsai, S.A. Chala, A.W. Kahsay, M.-H. Yeh, H.-M. Chen, A.D. Duma, H. Dai, B.-J. Hwang, Robust and conductive Magnéli Phase  $\text{Ti}_4\text{O}_7$  decorated on 3D-nanoflower NiRu-LDH as high-performance oxygen reduction electrocatalyst, *Nano Energy* 47 (2018) 309–315, <https://doi.org/10.1016/j.nanoen.2018.03.017>.
- [50] X. Han, L. An, Y. Hu, Y. Li, C. Hou, H. Wang, Q. Zhang,  $\text{Ti}_3\text{C}_2$  MXene-derived carbon-doped  $\text{TiO}_2$  coupled with  $\text{g-C}_3\text{N}_4$  as the visible-light photocatalysts for photocatalytic  $\text{H}_2$  generation, *Appl. Catal. B Environ.* 265 (2020), <https://doi.org/10.1016/j.apcatb.2019.118539>.
- [51] G. Yang, Y. Jiao, H. Yan, Y. Xie, A. Wu, X. Dong, D. Guo, C. Tian, H. Fu, Interfacial engineering of  $\text{MoO}_3$ -FeP heterojunction for highly efficient hydrogen evolution coupled with biomass electrooxidation, *Adv. Mater.* 32 (2020), e2000455, <https://doi.org/10.1002/adma.202000455>.
- [52] Y.-Y. Yang, X.-G. Zhang, C.-G. Niu, H.-P. Feng, P.-Z. Qin, H. Guo, C. Liang, L. Zhang, H.-Y. Liu, L. Li, Dual-channel charges transfer strategy with synergistic effect of Z-scheme heterojunction and LSPR effect for enhanced quasi-full-spectrum photocatalytic bacterial inactivation: new insight into interfacial charge transfer and molecular oxygen activation, *Appl. Catal. B Environ.* 264 (2020), 118465, <https://doi.org/10.1016/j.apcatb.2019.118465>.
- [53] R. Tang, S. Zhou, C. Li, R. Chen, L. Zhang, Z. Zhang, L. Yin, Janus-structured  $\text{Co-Ti}_3\text{C}_2$  MXene quantum dots as a Schottky catalyst for high-performance photoelectrochemical water oxidation, *Adv. Funct. Mater.* 30 (2020) 2000637, <https://doi.org/10.1002/adfm.202000637>.
- [54] Y. Wei, D. Wu, C. Yong, Z. Wang, P. Zhong, J. Qiu, J. Fan, J. Sun, Y. Lei, X. Wu, Robust and highly conductive  $\text{Ti}_4\text{O}_7$ /MXene nanocomposites as high-performance and long cyclic stability oxygen reduction electrocatalysts, *Appl. Surf. Sci.* 607 (2023), 154929, <https://doi.org/10.1016/j.apsusc.2022.154929>.
- [55] P. Gayen, C. Chen, J.T. Abiad, B.P. Chaplin, Electrochemical oxidation of atrazine and clothianidin on Bi-doped  $\text{SnO}_2\cdot\text{Ti}_n\text{O}_{2n-1}$  electrocatalytic reactive electrochemical membranes, *Environ. Sci. Technol.* 52 (2018) 12675–12684, <https://doi.org/10.1021/acs.est.8b04103>.
- [56] M. Passananti, F. Temussi, M.R. Iesce, G. Mailhot, M. Brigante, The impact of the hydroxyl radical photochemical sources on the rivastigmine drug transformation in mimic and natural waters, *Water Res.* 47 (2013) 5422–5430, <https://doi.org/10.1016/j.watres.2013.06.024>.
- [57] Y. Jing, B.P. Chaplin, Mechanistic study of the validity of using hydroxyl radical probes to characterize electrochemical advanced oxidation processes, *Environ. Sci. Technol.* 51 (2017) 2355–2365, <https://doi.org/10.1021/acs.est.6b05513>.
- [58] L. Jin, S. You, N. Ren, B. Ding, Y. Liu, Mo vacancy-mediated activation of peroxymonosulfate for ultrafast micropollutant removal using an electrified MXene filter functionalized with Fe single atoms, *Environ. Sci. Technol.* 56 (2022) 11750–11759, <https://doi.org/10.1021/acs.est.2c03904>.
- [59] J. Cai, M. Zhou, Y. Pan, X. Du, X. Lu, Extremely efficient electrochemical degradation of organic pollutants with co-generation of hydroxyl and sulfate radicals on Blue- $\text{TiO}_2$  nanotubes anode, *Appl. Catal. B Environ.* 257 (2019), 117902, <https://doi.org/10.1016/j.apcatb.2019.117902>.
- [60] N.T. Suen, S.F. Hung, Q. Quan, N. Zhang, Y.J. Xu, H.M. Chen, Electrocatalysis for the oxygen evolution reaction: recent development and future perspectives, *Chem. Soc. Rev.* 46 (2017) 337–365, <https://doi.org/10.1039/c6cs00328a>.
- [61] H. Li, W. Yang, L. Ma, G. Liu, Y. Yu, J. Cao, R. Zhu, W. Chen, Z. Yu, H. Long, K. Zhou, Q. Wei, 3D-printed highly ordered Ti networks-based boron-doped diamond: An unprecedented robust electrochemical oxidation anode for decomposition of refractory organics, *Chem. Eng. J.* 426 (2021), 131479, <https://doi.org/10.1016/j.cej.2021.131479>.
- [62] B. Jiang, Y. Tian, Z. Zhang, Z. Yin, L. Feng, Y. Liu, L. Zhang, Degradation behaviors of Isopropylphenazone and Aminopyrine and their genetic toxicity variations during UV/chloramine treatment, *Water Res.* 170 (2020), 115339, <https://doi.org/10.1016/j.watres.2019.115339>.
- [63] S. Patton, W. Li, K.D. Couch, S.P. Mezyk, K.P. Ishida, H. Liu, Impact of the ultraviolet photolysis of monochloramine on 1,4-dioxane removal: New insights into potable water reuse, *Environ. Sci. Technol. Lett.* 4 (2017) 26–30, <https://doi.org/10.1021/acs.estlett.6b00444>.
- [64] L. Wang, J. Lu, L. Li, Y. Wang, Q. Huang, Effects of chloride on electrochemical degradation of perfluorooctanesulfonate by Magnéli phase  $\text{Ti}_4\text{O}_7$  and boron doped diamond anodes, *Water Res.* 170 (2020), 115254, <https://doi.org/10.1016/j.watres.2019.115254>.